A Diagnostic Study of Jet Streaks: Kinematic Signatures and Relationship to Coherent Tropopause Disturbances

MATTHEW E. PYLE,* DANIEL KEYSER, AND LANCE F. BOSART

Department of Earth and Atmospheric Sciences, The University at Albany, State University of New York, Albany, New York

(Manuscript received 21 November 2002, in final form 17 June 2003)

ABSTRACT

A diagnostic study is conducted of the kinematics and evolution of upper-level jet streaks representative of three (of the four) phases in the Shapiro conceptual model of a jet streak progressing through a synoptic-scale baroclinic wave over North America. The three phases selected for consideration apply to those segments of the wave pattern where jet streaks are relatively straight. The 1200 UTC 2 December 1991 case (trough-over-ridge) considers a strong jet streak located over eastern North America and constitutes the bulk of the study; the other two cases, which also concern jet streaks over North America, are from 0000 UTC 11 November 1995 (northwesterly flow) and 0000 UTC 28 October 1995 (southwesterly flow). Kinematic signatures consistent with the classic four-quadrant conceptual model for a straight jet streak are evident in all three cases, although flow curvature and thermal advection lead to significant departures from this conceptual model. The position of the jet streak within the synoptic-scale flow pattern also is shown to have a discernible influence on the kinematic fields, adding to the more localized effects of flow curvature and thermal advection in causing observed jet-streak kinematic signatures to depart from the four-quadrant conceptual model.

The investigation of the evolution of the trough-over-ridge jet streak focuses on a vortexlike feature situated on the cyclonic-shear side of the jet streak and manifested as a localized mesoscale depression in the height of the dynamic tropopause (DT), corresponding to a local maximum of pressure on the DT. Complementary signatures of this vortexlike feature, referred to as a coherent tropopause disturbance (CTD), are a local minimum in potential temperature on the DT and a maximum in potential vorticity (PV) on tropopause-intersecting isentropic surfaces. In the trough-over-ridge case, a CTD is tracked for 17.5 days during which time it influences not only the jet streak considered for kinematic study but also one additional jet streak. The evolutions of the northwesterly and southwesterly flow jet streaks are also evaluated in relation to their association or lack thereof with CTDs. The northwesterly flow jet streak intensifies in the absence of a CTD, whereas the southwesterly flow jet streak is associated with a CTD that is tracked for 11.5 days and that participates in the intensification of one additional jet streak. In all three cases, the jet streaks coincide with large horizontal gradients of pressure and potential temperature on the DT and of PV on tropopause-intersecting isentropic surfaces. In the two cases involving CTDs, their role is to enhance these respective gradients over a mesoscale region; this enhancement appears to focus and strengthen jet-streak winds over the same region, suggesting the importance of CTDs in jet-streak evolution.

1. Introduction

Jet streaks, defined as localized wind speed maxima within jet streams (e.g., Palmén and Newton 1969, p. 199; Bluestein 1993, section 2.7.4), are a classic topic in midlatitude synoptic–dynamic meteorology. Studies relating upper-level jet streaks to cyclogenesis (e.g., Bjerknes 1951; Uccellini et al. 1984, 1987; Uccellini and Kocin 1987; Wash et al. 1988; Velden and Mills 1990), severe weather (e.g., Beebe and Bates 1955; Uccellini and Johnson 1979; Bluestein and Thomas 1984), and the mesoscale enhancement of precipitation (e.g., Cahir 1971; Uccellini and Kocin 1987; Hakim and Uccellini 1992) have been conducted for a number of decades. Conceptual models depicting jet-streak kinematic signatures in various flow configurations also have a long record in the literature (e.g., Namias and Clapp 1949; Bjerknes 1951; Beebe and Bates 1955; Shapiro 1982). In addition to receiving scrutiny from the preceding significant-weather and kinematic perspectives, jet streaks and associated upper-level frontal zones have been the subject of conceptual models that describe the evolution of a jet streak or jet front (so named to emphasize the frequent connection between jet streaks and upper-level fronts) as it passes through a Rossby wave regime (e.g., Riehl et al. 1952; Shapiro 1982; Schultz and Doswell 1999).

* Current affiliation: Science Applications International Corporation, Beltsville, Maryland.

Corresponding author address: Dr. Daniel Keyser, Dept. of Earth and Atmospheric Sciences, The University at Albany, State University of New York, ES-224, Albany, NY 12222.
E-mail: keyser@atmos.albany.edu

The present study applies modern diagnostic tools to observed cases to evaluate the extent to which several of the above longstanding conceptual models regarding jet-streak kinematics and evolution can be verified. The primary emphasis is on straight jet streaks, motivated by the widespread application of the ''four-quadrant'' representation of upper-tropospheric horizontal divergence and midtropospheric vertical motion about a straight jet streak. In the straight jet-streak conceptual model (see, e.g., Uccellini and Kocin 1987, Fig. 3), upper-level divergence is found on the anticyclonic-shear (AS) side of the jet-streak entrance region and on the cyclonic-shear (CS) side of the jet-streak exit region; upper-level convergence is found on the CS side of the entrance region and on the AS side of the exit region. This configuration of upper-level divergence and convergence is accompanied by transverse ageostrophic circulations that are thermodynamically direct (indirect) in the entrance (exit) region of the jet streak, such that the upper-level ageostrophic wind is directed toward lower (higher) geopotential heights in the entrance (exit) region of the jet streak. The straight jet-streak conceptual model is first clearly formulated by Bjerknes (1951), although transverse ageostrophic circulations in jet-entrance and -exit regions are described earlier by Bjerknes and Holmboe (1944), and an idealized transverse circulation in a jet-entrance region is depicted by Namias and Clapp (1949, Fig. 4). A complementary formulation of the straight jet-streak conceptual model in terms of the thickness field is presented by Sutcliffe and Forsdyke (1950, Fig. 24), where lower-tropospheric cyclonic and anticyclonic development correspond to the aforementioned patterns of upper-tropospheric divergence and convergence, respectively.

Modifications to the straight jet-streak conceptual model are introduced by flow curvature and thermal advection: both of these processes alter the spatial distribution of divergence and vertical motion in the vicinity of a jet streak. The impact of flow curvature on upper-level divergence patterns in the vicinity of jet streaks is discussed by Bjerknes and Holmboe (1944), and Beebe and Bates (1955) depict the kinematic signature of a cyclonically curved jet streak at the base of a trough. The schematic of Beebe and Bates (1955, Fig. 4b) treats the upper-level divergence associated with a cyclonically curved jet streak as a superposition of the two-cell divergence pattern associated with uniform flow through a wave onto the four-cell divergence pattern associated with parcel accelerations into and out of a jet streak. This qualitative simplification has support from modeling studies by Newton and Trevisan (1984) and Moore and VanKnowe (1992). Alterations to the upper-level divergence pattern in the vicinity of jet streaks introduced by flow curvature are discussed further by Keyser and Shapiro (1986, section 4b). Idealized thermal advection patterns are considered by Shapiro (1982), with cases having a small angle between the isotherms and the longitudinal axis of the jet streak (Shapiro 1982, Figs. 6c,d) most relevant to the present study. In these cases, cold (warm) advection is anticipated to shift the entrance-region transverse ageostrophic circulation toward the AS (CS) side of the jet streak and to shift the exit-region transverse ageostrophic circulation toward the CS (AS) side of the jet streak. Examples of laterally displaced circulations in the presence of thermal advections consistent with the Shapiro (1982) model are provided by Cammas and Ramond (1989) for cases of cold (warm) advection in a jet-streak entrance (exit) region, and by Lackmann et al. (1997) for a case of cold advection in a jet-streak exit region.

Studies investigating the origin and evolution of jet streaks are comparatively few in number. Only recently has the conceptual model of Shapiro (1982, Fig. 7) of the progression of a jet streak through a synoptic-scale baroclinic wave situated over North America begun to be evaluated in the context of observed cases (Schultz and Doswell 1999). Previous studies have documented the shorter-term evolution of jet streaks, typically in relation to cyclogenesis (e.g., Uccellini et al. 1984, 1985), but the present paper will emphasize their evolution on the broader temporal and spatial scales addressed by the Shapiro (1982) model. Our experience in documenting the evolution of jet streaks has fostered the viewpoint that these features (represented as wind speed maxima) are not inherently trackable. Although some jet streaks can be tracked over multiday periods, the signature of the wind speed maximum can become obscured or ambiguous, particularly when the jet streak migrates through an amplified wave pattern. Downstream baroclinic development studies (e.g., Orlanski and Sheldon 1995, section 3) have shown that ageostrophic geopotential fluxes can be used to track the downstream dispersion of eddy kinetic energy (EKE) even when the continuous progression of a wind speed maximum through a wave pattern is difficult to detect. The present study follows this line of thought by posing the hypothesis that jet streaks are transient and that their evolution is a manifestation of fundamental structures and mechanisms involved in the dynamics of the extratropical tropopause: the class of Rossby waves that propagate and disperse along the Ertel potential vorticity (PV) gradients on tropopause-intersecting isentropic surfaces, and vortexlike structures based on the dynamic tropopause (DT), to be referred to as coherent tropopause disturbances (CTDs).

A CTD is manifested as a localized mesoscale depression in the height of the DT, as well as a local minimum in potential temperature on the DT and maximum in PV on tropopause-intersecting isentropic surfaces. CTDs are characterized further by their longevity with respect to the lifetime of an individual jet streak and by their confinement or trapping of air parcels. Hakim (2000) and references therein describe the dynamical properties of CTDs and establish how they differ from quasi-linear Rossby waves. The relationship between CTDs and jet streaks has been investigated recently by Bosart et al. (1996), Lackmann et al. (1997), Cunningham and Keyser (2000), Hakim (2000), Donnadille et al. (2001b), and Meade (2001). The fundamental idea is that these DT-based disturbances may act as a focusing mechanism for jet streaks by strengthening horizontal PV gradients on tropopause-intersecting isentropic surfaces. The connection between strong PV gradients and jet structures has been discussed by Davies and Rossa (1998), Morgan and Nielsen-Gammon (1998), and Nielsen-Gammon (2001).

In the remainder of this paper, a diagnostic study is presented of the kinematics and evolution of upper-level jet streaks representative of three (of the four) phases in the Shapiro conceptual model of the progression of a jet streak through a synoptic-scale baroclinic wave. The three phases apply to those segments of the wave pattern where jet streaks are relatively straight: trough-over-ridge (1200 UTC 2 December 1991), northwesterly flow (0000 UTC 11 November 1995), and southwesterly flow (0000 UTC 28 October 1995). Section 2 describes the diagnostics used to examine the jet-streak kinematics and introduces the dynamical quantities used to study jet-streak evolution. Section 3 examines the kinematic signatures of the three cases in relation to various idealized conceptual models, and section 4 investigates jet-streak evolution in relation to CTDs and Rossby waves. Section 5 summarizes the primary findings of this study and outlines several potential directions for future research.

2. Data and methodology

The three jet streaks considered in this paper were identified through a subjective survey of operational 300-hPa analyses over North America produced by the National Centers for Environmental Prediction for the cool seasons contained within the period from October 1990 through March 1996. Diagnostic study of the kinematics and evolution of these jet streaks is conducted using uninitialized global analyses of horizontal wind, pressure coordinate vertical velocity, temperature, and geopotential height generated every 6 h by the European Centre for Medium-Range Weather Forecasts (ECMWF) and obtained from the National Center for Atmospheric Research. The ECMWF data are stored as spherical harmonics and upon transformation to physical space reside on a 1.125° latitude–longitude grid. The data subsequently are interpolated onto limited-area diagnostic domains used in the kinematic and evolution studies; the specifications for these domains are provided in the following subsections. Mandatory-level data at 1000, 850, 700, 500, 400, 300, 250, 200, 150, 100, and 50 hPa are interpolated linearly with respect to the logarithm of pressure as necessary to provide data at 50-hPa intervals between 1000 and 50 hPa. The General Meteorological Package (GEMPAK; desJardins et al. 1995) is used for calculation of selected diagnostics and for visualization of the gridded datasets on display domains consisting of subsets of the diagnostic domains.

a. Kinematic methodology

For the kinematic portion of this study, the data are interpolated onto diagnostic domains defined by Lambert conformal projections (e.g., Saucier 1955, section 2.13) true at 30° and 60°N with a horizontal grid spacing of 100 km. This grid spacing is similar to that of the original dataset and resolves adequate detail at the scales of interest for this study. The diagnostic software package described by Loughe et al. (1995, hereafter LLK) and known as SUNYPAK is used to derive the kinematic fields described in this subsection. (Real-time diagnostics created using SUNYPAK software along with the source code are available on the Web at http://www.atmos.albany.edu/deas/sunypak1.html.) A simplifying assumption of SUNYPAK is the use of a constant Coriolis parameter, rendering the geostrophic wind nondivergent. The value of the Coriolis parameter is determined from the latitude at the center of each diagnostic domain. The diagnostic domain for the December 1991 trough-over-ridge case comprises 100 × 80 points in the x and y directions and is centered at 45°N, 75°W. The other two cases utilize 80 × 80 point diagnostic domains: the domain for the November 1995 northwesterly flow case is centered at 47.5°N, 110°W, and the domain for the October 1995 southwesterly flow case is centered at 42.5°N, 82.5°W.

The three-component Helmholtz decomposition of the horizontal wind on limited-area domains proposed by Lynch (1989) and adapted to the ageostrophic wind by LLK is implemented in this study. In this decomposition, the total ageostrophic wind ($\mathbf{V}_{ag}$) is separated into harmonic ($\mathbf{V}_{agh}$), rotational ($\mathbf{V}_{agr}$), and divergent ($\mathbf{V}_{agd}$) parts. The harmonic part, which is both nondivergent and irrotational, is defined in LLK in terms of a velocity potential. The harmonic velocity potential is determined using a Dirichlet boundary condition provided by the tangential ageostrophic wind evaluated along the lateral boundaries of the diagnostic domains. The contribution of the harmonic part of the ageostrophic wind is effectively eliminated in the interior portions of the diagnostic domains by using relatively large domains selected such that the lateral boundaries coincide with regions of weak ageostrophic wind; accordingly, only the rotational and divergent parts are shown in subsequent decompositions of the ageostrophic wind. The rotational and divergent parts of the ageostrophic wind are formulated in terms of streamfunction and velocity potential, respectively, in conjunction with homogeneous lateral boundary conditions.

This study utilizes three representations of the pressure coordinate vertical velocity, ω: the first is that available from the ECMWF dataset and is referred to as the analyzed ω. The second, referred to as the kinematic ω, is obtained from an upward integration of the continuity equation [LLK, Eq. (2.2)], assuming zero vertical velocity at the lower boundary of the diagnostic domain (1000 hPa) and applying a linear correction to the horizontal divergence that yields zero vertical velocity at the upper boundary (50 hPa) (O'Brien 1970). The third representation, the so-called QG ω, is determined from an adiabatic, frictionless version of the quasigeostrophic (QG) ω equation with the forcing expressed in terms of the divergence of the Q vector (hereafter denoted as $\mathbf{Q}$) [LLK, Eq. (2.24)]; ω equals zero at the lower and upper boundaries of the diagnostic domain, and the kinematic ω is applied at the lateral boundaries.

The QG ω is partitioned into components ω_s and ω_n, which are attributed to the along-isentrope ($\mathbf{Q}_s$) and cross-isentrope ($\mathbf{Q}_n$) components of $\mathbf{Q}$, respectively. This decomposition of $\mathbf{Q}$ is based on a natural coordinate system specified by the potential temperature field on isobaric surfaces; background on the formulation of this coordinate system and examples of its application may be found in Keyser et al. (1988, 1992), Kurz (1992), and Barnes and Colman (1993, 1994). Solution of the QG ω equation for ω_s and ω_n assumes that these quantities equal zero on the lower, upper, and lateral boundaries. In this study, ω_s is taken to represent the vertical branch of the longitudinal vertical circulation attributable to flow curvature, and ω_n the vertical branch of the transverse vertical circulation related to parcel accelerations into and out of a jet streak, signified by confluence in the entrance region and diffluence in the exit region.[1]

The psi vector (hereafter denoted as $\boldsymbol{\psi}$) [Keyser et al. 1989; LLK, Eq. (2.17)] provides a compact representation of the three-dimensional divergent ageostrophic circulation. In this study, $\boldsymbol{\psi}$ is calculated from the kinematic ω field [LLK, Eqs. (2.18) and (2.19a)] and is then used to project the divergent ageostrophic circulation onto vertical cross sections oriented tangent and normal to the axis of a jet streak. This circulation is denoted as (v_{agdx}, ω_x), where, in the present context, x is the horizontal coordinate axis in the cross-section plane, $v_{\mathrm{agdx}} = -\partial\psi_x/\partial p$, and $\omega_x = \partial\psi_x/\partial x$.

b. Evolution methodology

For the evolution portion of this study, the data are interpolated onto an 85 × 85 point domain defined by a polar stereographic projection true at 60°N with a horizontal grid spacing of 200 km. The data subsequently are linearly interpolated from isobaric surfaces onto the DT, defined here in terms of an isosurface of Ertel PV, to create DT maps. For background on the construction and interpretation of DT maps, the reader is directed to the recent review by Nielsen-Gammon (2001) and references therein. An advantage of the DT perspective for this study is that it can portray features such as CTDs, which tend to be best defined in the vicinity of the tropopause, on a single map. On a DT map, a CTD is manifested as a local minimum in potential temperature; that is, the potential temperature field exhibits at least one closed contour. As a consequence of the conservation of potential temperature on the DT for adiabatic, frictionless flow, the appearance of at least one closed contour signifies the trapping of air parcels by the CTD. In addition to DT maps, maps of PV on isentropic surfaces (i.e., PV maps) are constructed to provide an alternative representation of CTDs and jet streaks, which coincide with local maxima of PV and strong gradients of PV on tropopause-intersecting isentropic surfaces, respectively. In constructing PV maps, Ertel PV is calculated directly on isentropic surfaces [$\mathrm{PV} = -g(\zeta_\theta + f)(\partial p/\partial\theta)^{-1}$; notation is standard] with $\partial p/\partial\theta$ evaluated over an 8-K-thick layer bracketing the surface under consideration.

The literature gives a range of values of PV [expressed in potential vorticity units (PVUs); 1 PVU = 10^{-6} m^2 s^{-1} K kg^{-1}] appropriate for defining the DT, typically between 1 and 3.5 PVU (e.g., Hoinka 1998; Morgan and Nielsen-Gammon 1998). In this study, the DT is defined as the uppermost 1.5-PVU surface located through a downward search of the PV field as a function of pressure starting at 50 hPa. Precedent for adopting the 1.5-PVU threshold to define the DT is found in related work on midlatitude cyclones (e.g., Davis and Emanuel 1991; Hakim et al. 1995; Bosart et al. 1996; Lackmann et al. 1997). Identifying and tracking CTDs is not anticipated to be highly sensitive to the actual PV threshold used to define the DT; this expectation is supported by the composites of extreme 500-hPa relative vorticity maxima calculated by Hakim (2000, section 5b), which are comparable with the CTDs examined in the present study. It may be inferred from the cross sections for Hakim's extreme composite that PV contours are closed (on isentropic surfaces) over a range between about 0.75 and 6 PVU, which brackets the 1.5-PVU threshold adopted to define the DT.

The definition of CTDs as local minima in the potential temperature field on the DT (θ_{trop}), motivated by the conservation of this quantity for adiabatic, frictionless flow, suggests its application for tracking CTDs. Nevertheless, our experience is that CTDs are more readily identified as localized depressions in the height of the DT, corresponding to local maxima of pressure on the DT (p_{trop}). Accordingly, p_{trop} is adopted as the primary variable for tracking CTDs, despite its nonconservation on the DT for adiabatic, frictionless flow. In this study, attention is focused on two CTDs: the first

[1] An alternative partition of ω based on a decomposition of $\mathbf{Q}$ in terms of a natural coordinate system specified by the geopotential height field [Jusem and Atlas (1998); refer to Donnadille et al. (2001a) for an application to an upper-level jet front] yields individual terms that isolate components of ω attributable to confluence/diffluence, flow curvature, and thermal advection. Although directly applicable to this study, the authors did not become aware of the Jusem–Atlas Q-vector partition until after the completion of the diagnostic calculations for the kinematic analysis to be presented in section 3.

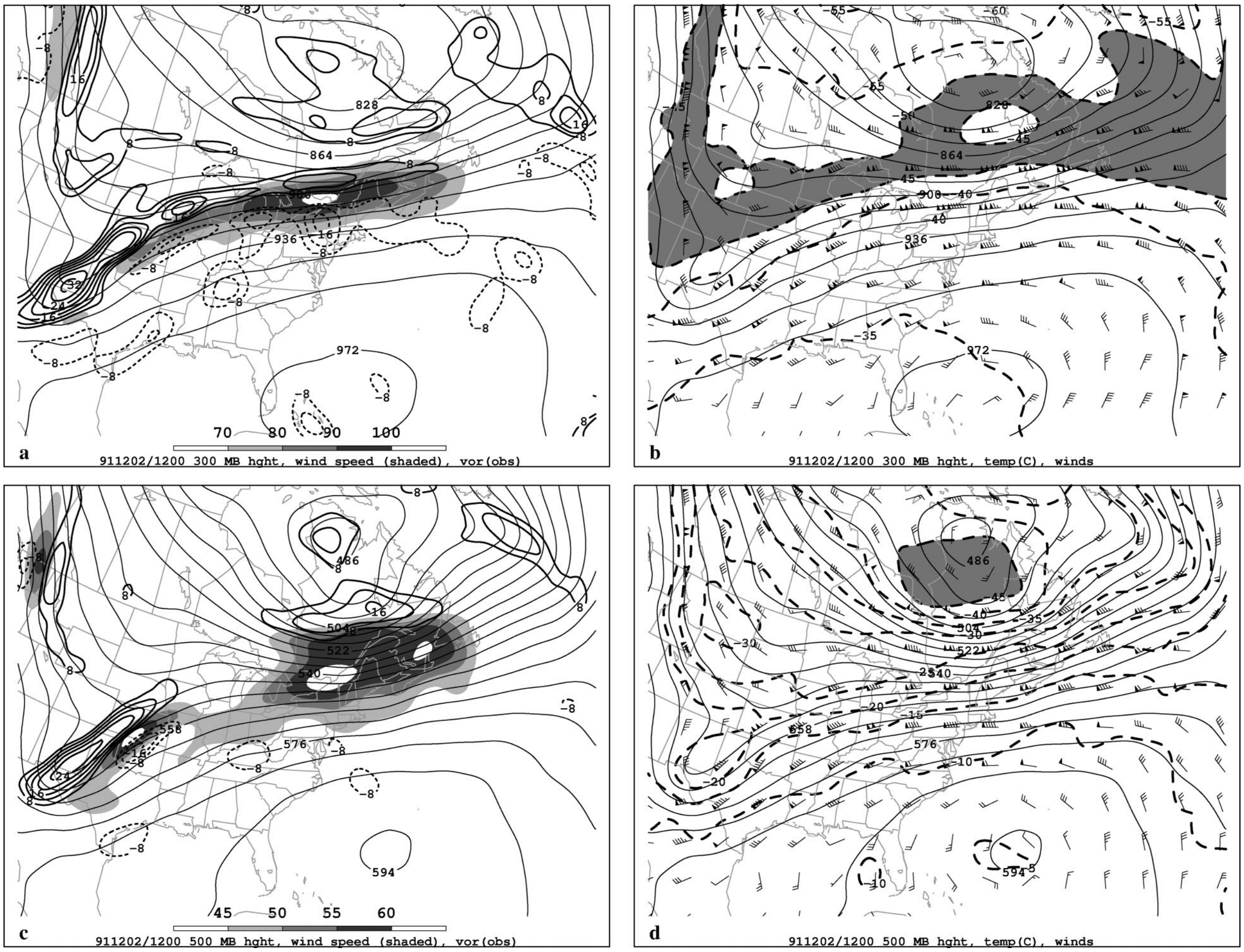

FIG. 1. Upper- and middle-tropospheric overview for 1200 UTC 2 Dec 1991: (a) 300-hPa geopotential height (thin solid; contour interval, 12 dam), relative vorticity [thick solid (positive) and dashed (negative); contour interval, 4×10^{-5} s^{-1}; zero and ± 4 contours suppressed], and horizontal wind speed (shaded as indicated for values greater than 70 m s^{-1}); (b) 300-hPa geopotential height [contoured as in (a)], temperature (thick dashed; contour interval, 5°C; shaded for values between $-50°$ and $-45°$C), and horizontal winds (plotted at every fourth grid point using standard convention: pennant, full barb, and half barb denote 25, 5, and 2.5 m s^{-1}, respectively); (c) as in (a) except at 500 hPa with a geopotential height contour interval of 6 dam and horizontal wind speeds shaded as indicated for values greater than 45 m s^{-1}; (d) as in (b) except at 500 hPa with a geopotential height contour interval of 6 dam and temperature shaded for values less than $-45°$C.

is involved in the evolution of the trough-over-ridge jet streak analyzed from a kinematic perspective on 1200 UTC 2 December 1991, and the second in the evolution of the southwesterly flow jet streak analyzed on 0000 UTC 28 October 1995. Each CTD is tracked manually on p_{trop} maps (contoured at an interval of 40 hPa) both backward and forward at 12-h intervals (reduced to 6 h during rapid evolutions) from the times of kinematic interest for the respective jet streaks. In those instances where the CTDs are not clearly manifested as local maxima in the p_{trop} field, θ_{trop} and PV on selected isentropic surfaces are used to ascertain their positions. Additional details of the tracking procedure are documented in Pyle (1997, section 2.3).

3. Jet-streak kinematics

In this section, we present kinematic analyses of upper-level jet streaks illustrative of the three phases in the Shapiro conceptual model where jet streaks are relatively straight. In addition to diagnosing kinematic signatures consistent with the classic four-quadrant conceptual model for a straight jet streak, we will show that flow curvature and thermal advection contribute to departures from this basic conceptual model, as does the position of the jet streak within the synoptic-scale flow pattern.

a. Trough-over-ridge case: 1200 UTC 2 December 1991

The basic synoptic features of the jet streak over eastern North America at 1200 UTC 2 December 1991 are shown in Fig. 1. The analyzed wind speed at 300 hPa (Fig. 1a) exceeds 100 m s^{-1} over a small region, and the jet streak is situated in a trough-over-ridge pattern with strong confluence upstream and diffluence downstream from the jet core. The geopotential height field (Fig. 1a) shows weak cyclonic curvature through the jet core, with stronger curvature closer to the 300-hPa low center on the CS side of the jet streak. The 300-hPa temperature field (Fig. 1b) exhibits a strong gradient poleward of the jet core; also important for later discussion is the localized warm pool southeast of Hudson Bay indicated by the closed contour of temperatures exceeding $-45°C$. This region of relative warmth, particularly when combined with the intense cold pool in approximately the same region at 500 hPa (Fig. 1d), is suggestive of the penetration of stratospheric air well below 300 hPa. Another thermal feature of interest is warm advection in the jet-streak exit region southeast of Newfoundland, particularly at 500 hPa (Fig. 1d).

The ageostrophic wind at 300 hPa (Fig. 2a) is directed toward lower (higher) geopotential heights in the jet-entrance (-exit) region, as anticipated from the straight jet-streak conceptual model reviewed in section 1. The rotational ageostrophic wind (Fig. 2b), which contributes significantly to the total ageostrophic wind (Fig. 2a) in the vicinity of the jet streak, displays prominent anticyclonic gyres flanking the core, and cyclonic gyres centered upstream from the entrance region and downstream from the exit region. This signature in the rotational ageostrophic wind may be related to the deficit or excess of the resultant deformation to the relative vorticity in a nondivergent barotropic framework [Cunningham and Keyser (2000); refer to their Eq. (8)]: resultant deformation less (greater) than the magnitude of the relative vorticity implies anticyclonic (cyclonic) gyres in the rotational ageostrophic flow. Strong ageostrophic flow directed across the geopotential height contours (i.e., cross-contour) is evident in the rotational ageostrophic wind within the entrance and exit regions (Fig. 2b). The divergent ageostrophic wind (Fig. 2c) is generally weaker than the rotational part, but contributes in the same sense as the rotational part to cross-contour ageostrophic flow within the entrance and exit regions (Fig. 2a). The dominance of the rotational part of the ageostrophic wind over the divergent part in the vicinity of the jet streak, evident in comparing Figs. 2b and 2c (note that the contour interval for the streamfunction is twice that for the velocity potential), is consistent with the results of previous related studies (e.g., Krishnamurti 1968; Keyser et al. 1989, 1992; LLK; Cunningham and Keyser 2000).

Figure 3 shows ω fields at 500 hPa, where the various representations of these fields generally attain their largest magnitudes for this case. The kinematic and QG ω patterns (Figs. 3a,b) are more complex than the idealized four-cell pattern for a straight jet streak. The kinematic ω (Fig. 3a) shows strong ascent centered over southeastern Oklahoma; this region of ascent corresponds to the AS side of the broad jet-entrance region and to an area of widespread stratiform precipitation (not shown), the latter observation suggestive of a diabatic contribution to the ascent. Diabatic heating can reinforce and focus the ascending branches of jet-streak circulations

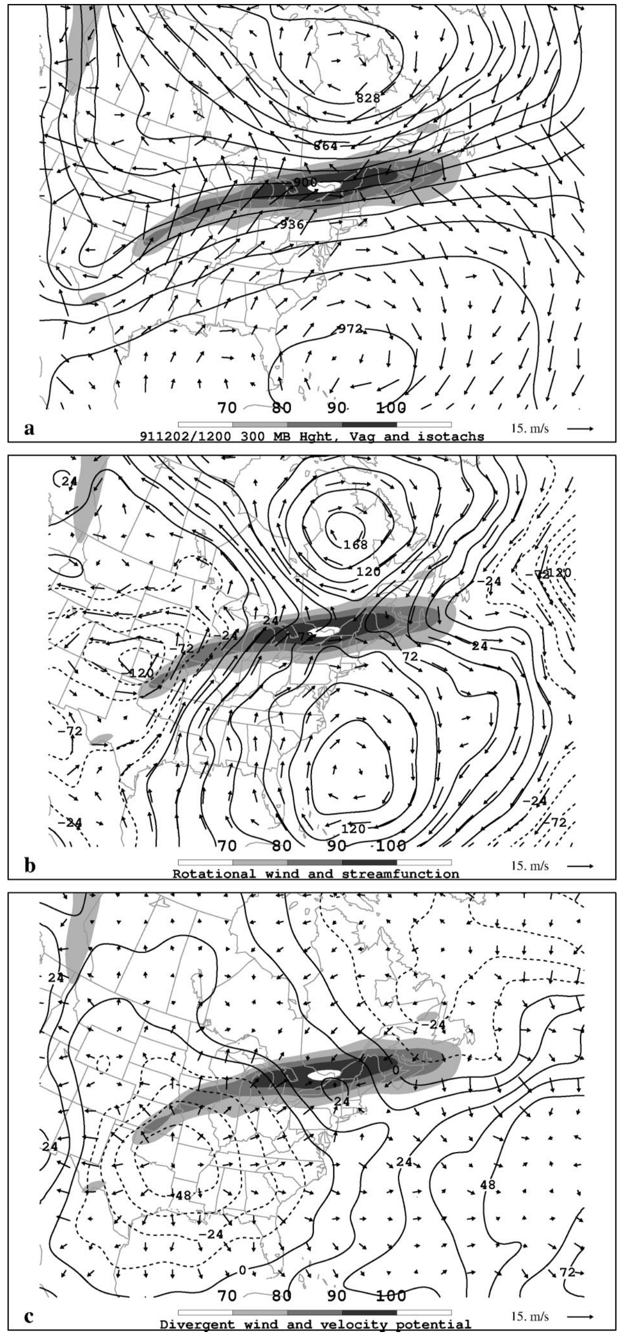

FIG. 2. Ageostrophic wind and components of the Helmholtz partition, along with total horizontal wind speed (shaded as indicated for values greater than 70 m s^{-1}), at 300 hPa for 1200 UTC 2 Dec 1991: (a) $\mathbf{V}_{ag}$ and geopotential height (contour interval, 12 dam), (b) $\mathbf{V}_{agr}$ and rotational streamfunction (contour interval, 24×10^5 m^2 s^{-1}), and (c) $\mathbf{V}_{agd}$ and divergent velocity potential (contour interval, 12×10^5 m^2 s^{-1}). Positive and zero contours are solid, negative contours are dashed, vectors are plotted at every third grid point, and a vector scale is given at the lower right of each panel.

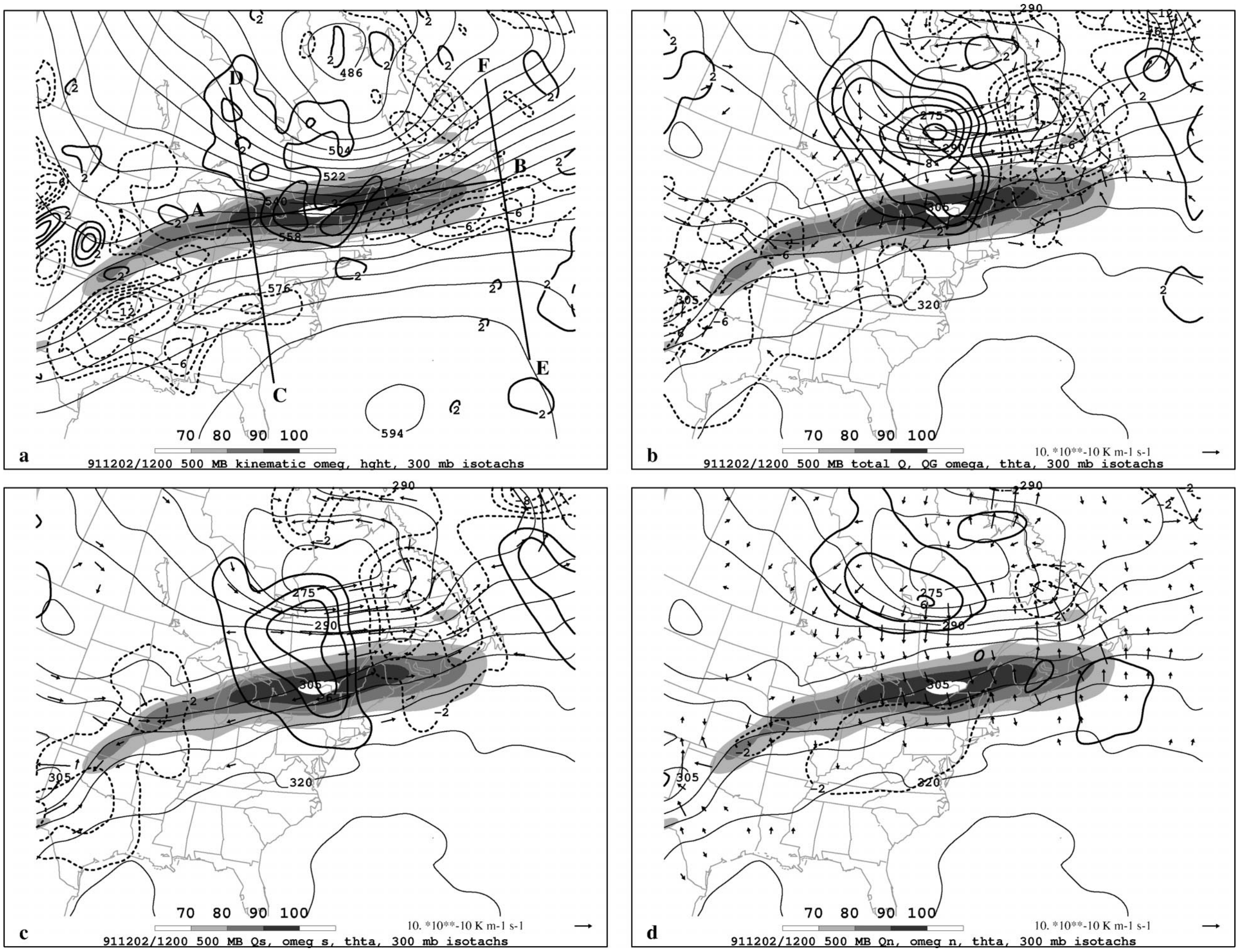

FIG. 3. Vertical motion diagnostics at 500 hPa, along with horizontal wind speed at 300 hPa (shaded as indicated for values greater than 70 m s^{-1}), for 1200 UTC 2 Dec 1991: (a) kinematic ω [thick solid (positive) and dashed (negative); contour interval, 2×10^{-1} Pa s^{-1}; zero contour suppressed], 500-hPa geopotential height (thin solid; contour interval, 6 dam), and locations of the cross sections displayed in Fig. 4 (thick lines labeled AB, CD, and EF, respectively); (b) $\mathbf{Q}$, total QG ω [contoured as for kinematic ω in (a)], and 500-hPa potential temperature (thin solid; contour interval, 5 K); (c) $\mathbf{Q}_s$, ω_s [contoured as for kinematic ω in (a)], and potential temperature as in (b); (d) $\mathbf{Q}_n$, ω_n [contoured as for kinematic ω in (a)], and potential temperature as in (b). Vectors are plotted at every other grid point and a vector scale is given at the lower right of (b), (c), and (d). Vectors with magnitudes less than 4×10^{-10} K m^{-1} s^{-1} in (b) and (c), and vectors with magnitudes less than 2×10^{-10} K m^{-1} s^{-1} in (d), are not plotted.

(e.g., Cahir 1971; Keyser and Johnson 1984; Chen and Dell'Osso 1987; Brill et al. 1991), yielding stronger and more localized ascent than would otherwise occur in adiabatic flow. The region of ascent centered over southeastern Oklahoma (Fig. 3a) coincides closely with the velocity potential minimum and the outflow center at 300 hPa (Fig. 2c). Middle-level ascent and upper-level divergence in this region are influenced by the shortwave trough immediately upstream, over eastern New Mexico–western Texas; note the relative vorticity maxima at 300 and 500 hPa (Figs. 1a,c). Subsidence extends upstream and poleward from the jet core, while downstream from the core there is a broad region of ascent that is maximized on the AS side of the exit region. The transition between descent and ascent is shifted slightly downstream from the jet core and coincides with the 500-hPa trough axis (Figs. 1c and 3a).

Despite significant differences in detail, the total QG ω (Fig. 3b) exhibits broad agreement with the kinematic ω (Fig. 3a). The QG ω field features ascent in the entrance region, although this area of ascent lacks the localized maximum over southeastern Oklahoma evident in the kinematic ω field. This absence is consistent with the hypothesized diabatic contribution to the ascent maximum noted above, since the version of the QG ω equation utilized in this study is adiabatic. The QG ω pattern is maximized on the CS side of the jet streak in the form of a descent–ascent dipole; inspection of the potential temperature field at 500 hPa (Fig. 3b) shows that the QG ω is largest along the strongest thermal

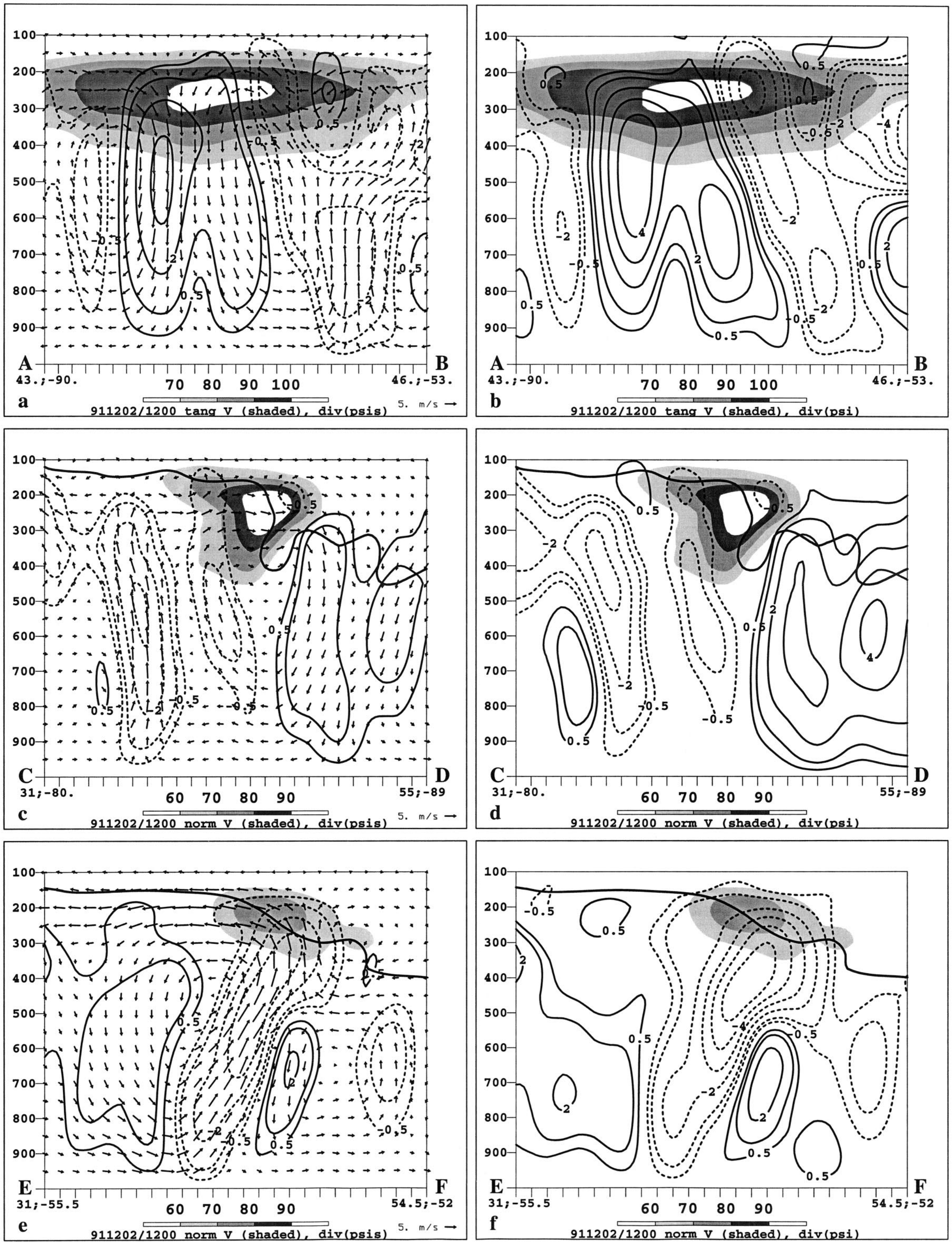
a
911202/1200 tang V (shaded), div(psis)
A
B
43.;-90.
46.;-53.
70 80 90 100
5. m/s
b
911202/1200 tang V (shaded), div(psi)
c
911202/1200 norm V (shaded), div(psis)
C
D
31;-80.
55;-89
60 70 80 90
d
911202/1200 norm V (shaded), div(psi)
e
911202/1200 norm V (shaded), div(psis)
E
F
31;-55.5
54.5;-52
f
911202/1200 norm V (shaded), div(psi)
100
200
300
400
500
600
700
800
900

gradient, consistent with the dependence of **Q** and QG ω on horizontal potential temperature gradients.

The maximum values of descent and ascent in the QG ω dipole (Fig. 3b) exceed those of the corresponding descent and ascent maxima in the kinematic ω field, which lie along the axis of and on the AS side of the jet streak (Fig. 3a). This excess is hypothesized to be related in part to the occurrence of stronger geostrophic than actual winds in the presence of cyclonic curvature; recall from Fig. 2a that the ageostrophic wind opposes the geostrophic wind in the region of the QG ω dipole. Stronger geostrophic than actual winds in this region might be expected to result in an overestimate of the vertical motion forcing due to its formulation in terms of the geostrophic flow in the QG system. Another factor contributing to the larger QG descent and ascent maxima compared with their kinematic counterparts is that the reference static stability (i.e., $-\partial\theta/\partial p$ averaged horizontally over the diagnostic domain; not shown) used in solving the QG ω equation is smaller than local values of static stability in the region of the QG ω dipole. The smaller reference static stability is consistent with the larger extrema in QG ω compared with kinematic ω, given the inverse proportionality between QG vertical motion and reference static stability [e.g., Hakim and Keyser (2001); refer to their Eq. (10)].

Figures 3c and 3d display distributions of **Q** and QG ω partitioned into along- and cross-isentrope components, respectively. The ω_s field exhibits a descent–ascent dipole, with the division between descent and ascent shifted downstream from the jet core toward the 500-hPa cutoff potential temperature minimum and trough axis. This dipole signature in ω_s is consistent with the presence of cyclonic curvature on the CS side of the jet streak. The ω_n field contains an asymmetric four-cell pattern, with larger magnitudes featured on the CS side of the jet streak where the magnitudes of $\mathbf{Q}_n$ are greater; other than the noted asymmetry, the four-cell pattern isolated in Fig. 3d agrees with the conceptual model for a straight jet streak discussed in section 1. Nevertheless, the dominance of $\mathbf{Q}_s$ over $\mathbf{Q}_n$ (cf. Figs. 3c and 3d) suggests that cyclonic curvature poleward of the jet streak has a stronger influence on the QG vertical motion than parcel accelerations in the entrance and exit regions, making $|\omega_s| > |\omega_n|$ and accounting for the dipole pattern in total QG ω on the CS side of the jet streak (Fig. 3b).

Cross sections (locations given in Fig. 3a) of the divergent ageostrophic circulation further illustrate the influence of the jet streak and its synoptic-scale environment on the vertical motion field. Figure 4a shows the projection of the divergent circulation (v_{agdx}, ω_x) onto the cross-section plane tangent to the axis of the jet streak. The circulation is centered slightly downstream from the jet core, consistent with the depiction of the kinematic ω field at 500 hPa (Fig. 3a). Figure 4b displays, in the same plane as in Fig. 4a, the total ω field determined from $\boldsymbol{\psi}$. The patterns of ω_x and total ω are similar, although the descent near the jet core and the ascent at upper levels in the exit region are much stronger in the latter, indicative of significant cross-jet contributions to the divergent ageostrophic circulation in these locations.

The divergent circulation in the cross-section plane normal to the jet-entrance region (Fig. 4c) is thermodynamically direct, and is centered beneath the jet core with ascent confined mainly to the equatorward side of the jet streak. The divergent ageostrophic circulation in the cross-jet direction accounts for most of the ascent in this plane, as seen by the similarity between ω_x and total ω equatorward of the jet core (cf. Figs. 4c and 4d). On the other hand, in the region of descent on the poleward side of the core, ω_x is less than the total ω, revealing a significant component of the divergent circulation in the along-jet direction. Comparison of ω_x (Fig. 4e) with the total ω (Fig. 4f) shows that the divergent ageostrophic circulation in the cross-section plane normal to the jet-exit region reproduces the total ω pattern, although ω_x underestimates the magnitudes of the descent and ascent maxima in the total ω. As in the comparison between Figs. 4c and 4d, this underestimate indicates the presence of a divergent circulation in the along-jet direction. Above 500 hPa, the region of ascent in ω_x corresponds to that found in the total ω on the downstream edge of the cross section tangent to the jet streak and discussed above in the comparison between Figs. 4a and 4b. The divergent circulation in the cross-section plane (Fig. 4e) is indirect and shifted significantly toward the equatorward (i.e., AS) side of the jet core. This shift is consistent with the conceptual

←

FIG. 4. Cross sections for 1200 UTC 2 Dec 1991 (locations given in Fig. 3a): (a) cross-section AB, oriented tangent to the axis of the jet streak with the horizontal wind component tangent to the cross section (v_x; shaded as indicated for values greater than 70 m s^{-1}) and the projection of the pressure coordinate vertical velocity onto the cross-section plane [$\omega_x = \partial\psi_x/\partial x$; solid (positive) and dashed (negative); contour interval, 1×10^{-1} Pa s^{-1}; ± 0.5 contours included and zero contour suppressed], overlaid with the circulation composed of divergent ageostrophic wind projected onto the cross-section plane in the horizontal ($v_{\mathrm{agdx}} = -\partial\psi_x/\partial p$) and ω_x in the vertical; (b) oriented as in (a) with v_x [shaded as in (a)] and the total pressure coordinate vertical velocity determined from $\boldsymbol{\psi}$ [$\omega = \boldsymbol{\nabla}_p \cdot \boldsymbol{\psi}$; contoured as for ω_x in (a)]; (c) as in (a) except for cross-section CD, oriented normal to the jet-entrance region with the horizontal wind component normal to the cross section (v_y; shaded as indicated for values greater than 60 m s^{-1}) and the 1.5-PVU contour (thick solid); (d) oriented as in (c) with v_y [shaded as in (c)], the 1.5-PVU contour (thick solid), and ω [contoured as for ω_x in (a)]; (e), (f) as in (c), (d) except for cross-section EF, oriented normal to the jet-exit region. A horizontal vector scale is given at the lower right of (a), (c), and (e). The vertical vector scale is approximately 2.8×10^{-1} Pa s^{-1} per 50 hPa vertical grid interval in (a) and 3.1×10^{-1} Pa s^{-1} per 50 hPa vertical grid interval in (c) and (e).

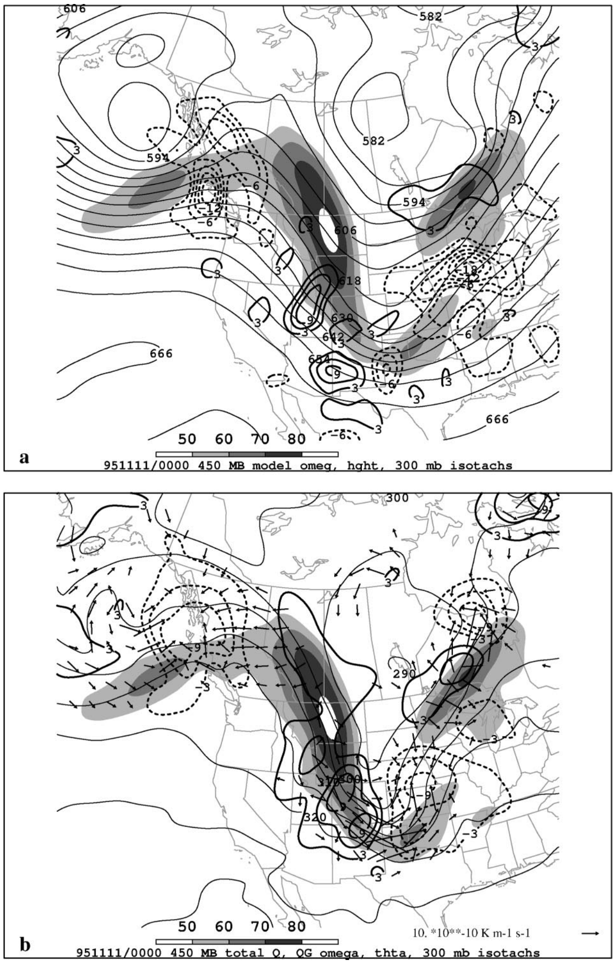

FIG. 5. Analyses for 0000 UTC 11 Nov 1995: (a) horizontal wind speed at 300 hPa (shaded as indicated for values greater than 50 m s^{-1}), along with geopotential height (thin solid; contour interval, 6 dam) and analyzed ω [thick solid (positive) and dashed (negative); contour interval, 3×10^{-1} Pa s^{-1}; zero contour suppressed] at 450 hPa; (b) horizontal wind speed as in (a), along with potential temperature (thin solid; contour interval, 5 K), QG ω [contoured as for analyzed ω in (a)], and **Q** at 450 hPa. Vectors are plotted at every other grid point and a vector scale is given at the lower right of (b). Vectors with magnitudes less than 4×10^{-10} K m^{-1} s^{-1} are not plotted.

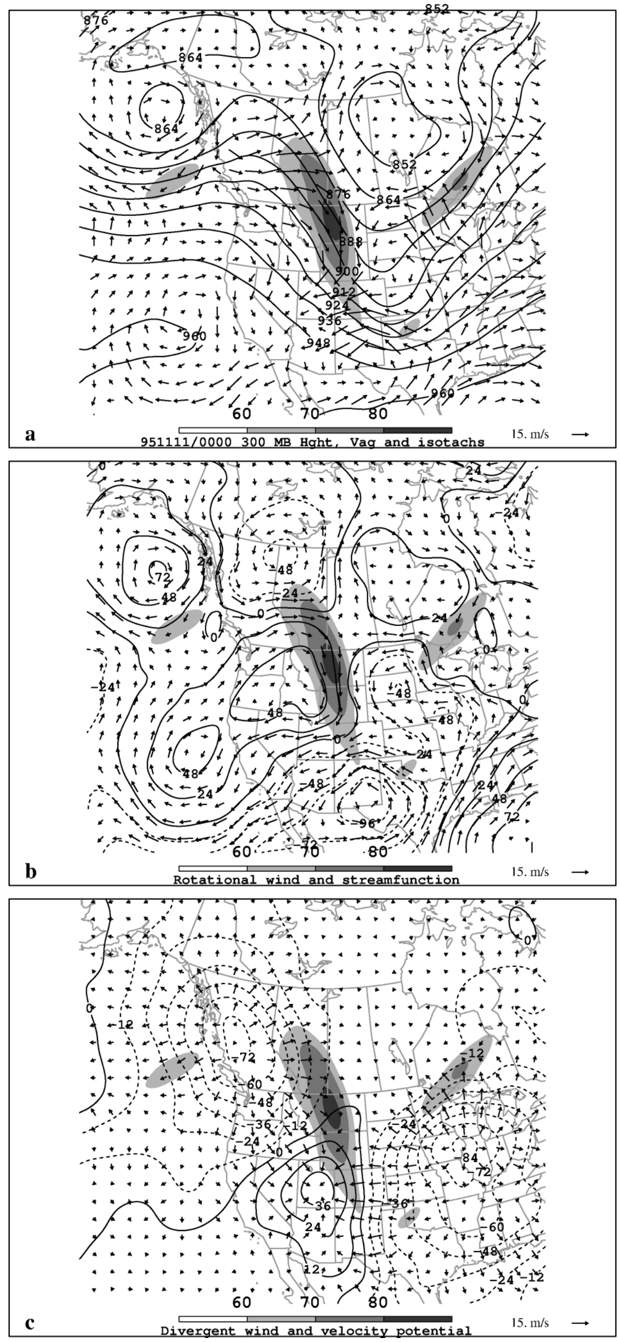

FIG. 6. As in Fig. 2 except at 0000 UTC 11 Nov 1995 with horizontal wind speed shaded as indicated for values greater than 60 m s^{-1} and vectors plotted at every other grid point.

model of Shapiro (1982) reviewed in section 1, given the presence of warm advection at 500 hPa in the exit region noted previously (Fig. 1d).

b. Northwesterly flow case: 0000 UTC 11 November 1995

The northwesterly flow jet streak, featuring a core of winds in excess of 80 m s^{-1} at 300 hPa, is located over the Intermountain West region in a complex synoptic pattern (Figs. 5a and 6a). The jet streak lies downstream from a short-wave ridge located over British Columbia and upstream from a short-wave trough located over the southern plains region. The ageostrophic wind at 300 hPa (Fig. 6a) shows cross-contour flow of the anticipated direction in the entrance and exit regions, with supergeostrophic flow through the jet core. The rotational part (Fig. 6b) contains cyclonic gyres centered upstream from the entrance region and downstream from the exit region, in agreement with the signature diagnosed in the trough-over-ridge case (Fig. 2b). Both the rotational and divergent parts make nearly equal contributions to cross-contour ageostrophic flow within the entrance and exit regions (Figs. 6b,c).

The analyzed and the QG ω fields are shown at 450 hPa (Figs. 5a,b), the approximate level of maximum vertical motion for the northwesterly flow case. Ascent is found over the west coast of Canada; this ascent occurs on the AS side of the jet-entrance region and downstream from the trough approaching the Canadian coast. Strong descent is maximized on the AS side of the jet-exit region in both the analyzed and the QG ω fields, with this descent extending toward the CS side of the entrance region in the latter. Ascent on the CS side of the exit region is absent from both of the ω fields; descent upstream from the southern plains trough may be suppressing the ascent expected over the exit region. Consistency with the straight jet-streak conceptual model essentially is restricted to the AS side, where the vertical motion signature attributable to confluence/diffluence is reinforced by vertical motion attributable to the synoptic-scale wave pattern.

c. *Southwesterly flow case: 0000 UTC 28 October 1995*

The southwesterly flow jet streak at 300 hPa is located between a broad trough over the central plains and a short-wave ridge over Quebec (Figs. 7a and 8a). The ageostrophic wind at 300 hPa (Fig. 8a) is strongly subgeostrophic through the base of the trough and directed toward lower geopotential heights within the entrance region; cross-contour ageostrophic flow in the exit region is confined to a relatively small area. Consistent with the previous cases, this jet streak exhibits cyclonic gyres in the rotational ageostrophic wind (Fig. 8b) upstream from the entrance region and downstream from the exit region, although the latter gyre is not as clearly defined as the former. The divergent ageostrophic wind (Fig. 8c) is strong across the entrance region of the southwesterly flow jet streak, but weak in the exit region.

Further evidence of the tendency for vertical motions in the neighborhood of jet streaks to conform to the expectations of the straight jet-streak conceptual model only in the absence of the counteracting influence of synoptic-scale vertical motion can be seen in the analyzed ω field at 400 hPa (Fig. 7a). Regions of strong ascent are situated on the AS side of the entrance region and on the CS side of the exit region of the southwesterly flow jet streak, but corresponding regions of descent are absent on the adjacent sides of the entrance and exit regions. This absence is consistent with the locations of the entrance region downstream from the broad trough and the exit region upstream from the short-wave ridge, such that the ascent attributable to these features masks the descent expected in the entrance and exit regions. An extensive region of convection occurring along an arc between Louisiana and southeastern Virginia and an area of stratiform precipitation centered over Quebec

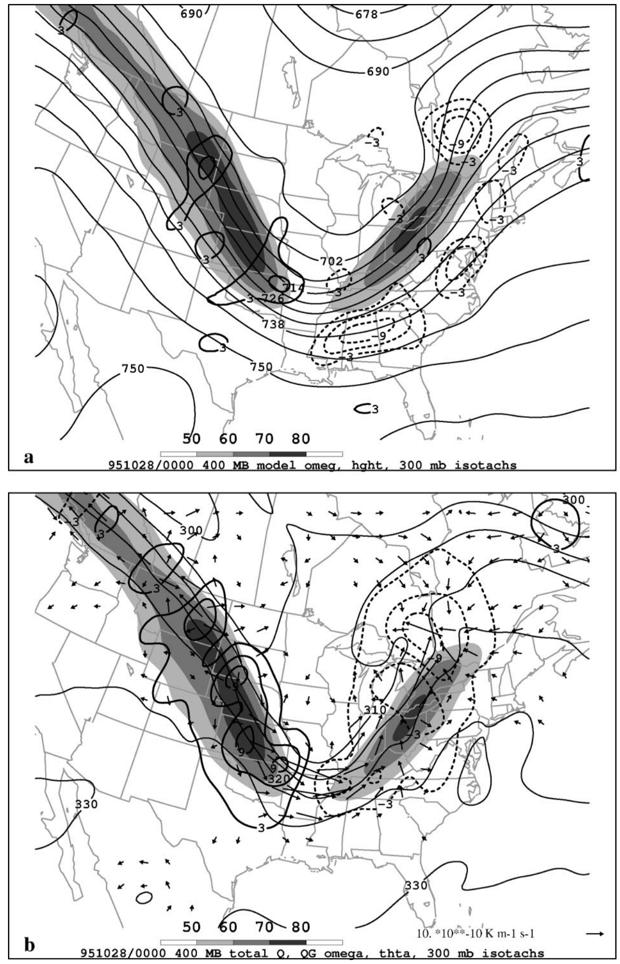

FIG. 7. Analyses for 0000 UTC 28 Oct 1995: (a) horizontal wind speed at 300 hPa (shaded as indicated for values greater than 50 m s^{-1}), along with geopotential height (thin solid; contour interval, 6 dam) and analyzed ω [thick solid (positive) and dashed (negative); contour interval, 3×10^{-1} Pa s^{-1}; zero contour suppressed] at 400 hPa; (b) horizontal wind speed as in (a), along with potential temperature (thin solid; contour interval, 5 K), QG ω [contoured as for analyzed ω in (a)], and **Q** at 400 hPa. Vectors are plotted at every other grid point and a vector scale is given at the lower right of (b). Vectors with magnitudes less than 4×10^{-10} K m^{-1} s^{-1} are not plotted.

[not shown; discussed in Pyle (1997, section 6.1)] likely are reinforcing ascent in the analyzed ω on the AS side of the entrance region and on the CS side of the exit region, respectively. The QG ω field at 400 hPa (Fig. 7b) also exhibits regions of strong ascent in the entrance and exit regions, although these features are not as localized as their analyzed counterparts and are shifted toward the CS side of the jet. These differences may be related to the neglect of diabatic heating in the version of the QG ω equation used in the present study.

4. Jet-streak evolution

In this section, we investigate jet-streak evolution in relation to CTDs and Rossby waves, with the relative

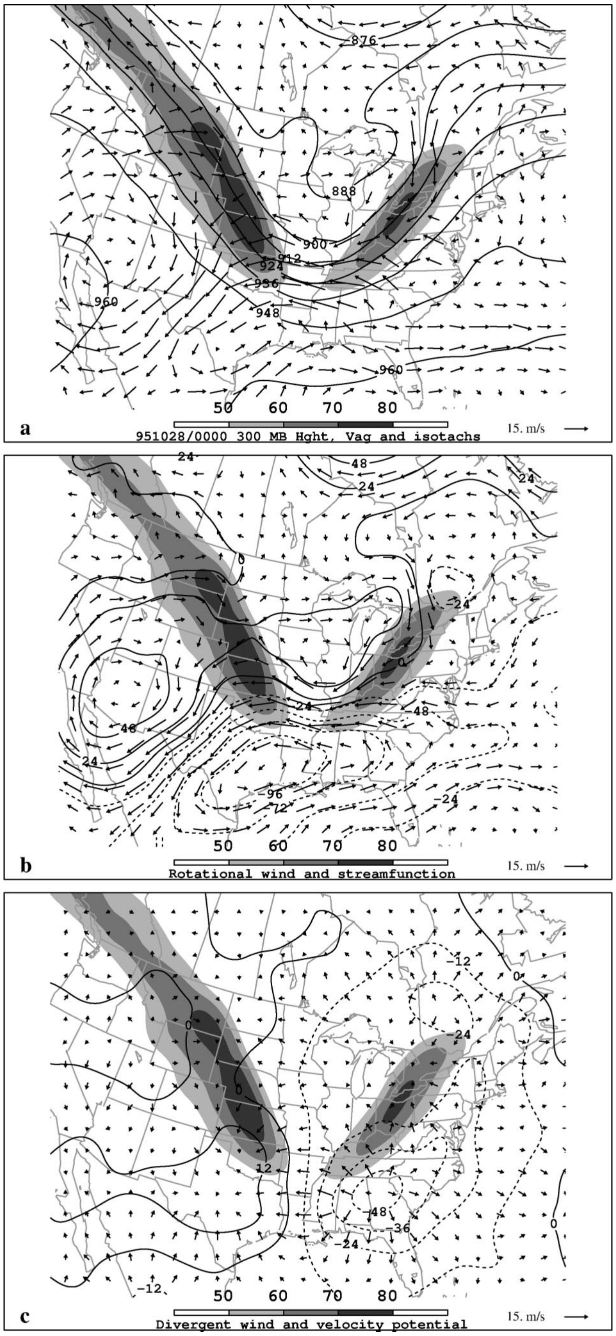

FIG. 8. As in Fig. 2 except at 0000 UTC 28 Oct 1995 with horizontal wind speed shaded as indicated for values greater than 50 m s^{-1} and vectors plotted at every other grid point.

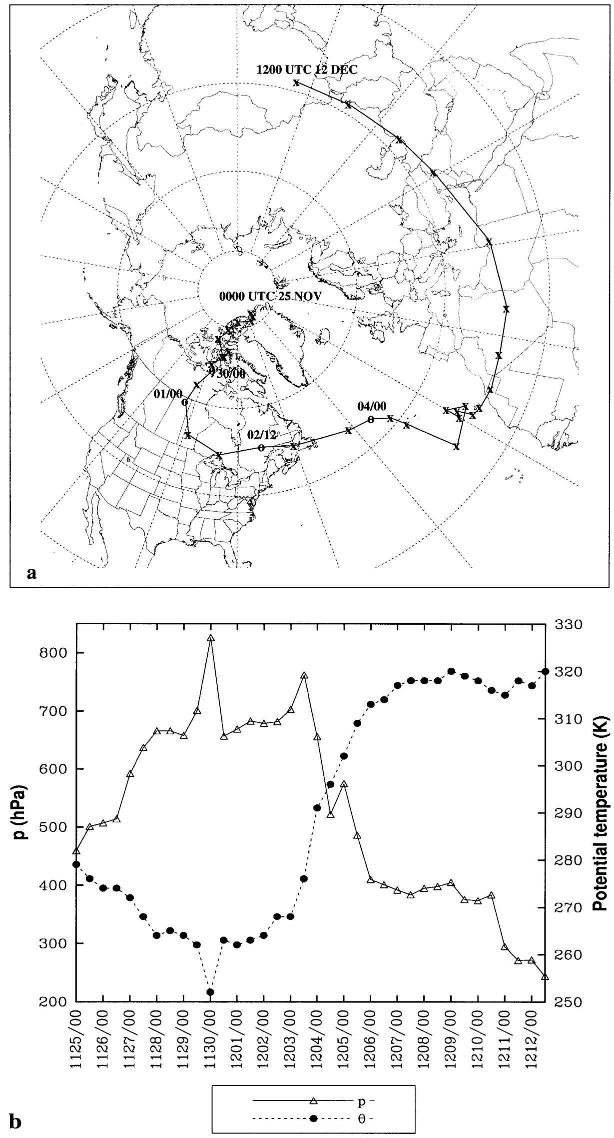

FIG. 9. Summary plots of the CTD associated with the trough-over-ridge jet streak: (a) track map with a bold x (o for times discussed in the text) marking the positions of the p_{trop} maximum of the CTD at 12-h intervals from its initiation at 0000 UTC 25 Nov 1991 to its termination at 1200 UTC 12 Dec 1991; and (b) time series of the p_{trop} maximum (hPa, open triangles) and θ_{trop} minimum (K, solid circles) associated with the CTD for the same time period as in (a). Note that the locations of the p_{trop} maximum and θ_{trop} minimum for the CTD are not necessarily coincident at a given time.

contributions of these respective features varying among the three cases documented in this study. The trough-over-ridge jet streak intensifies in response to the close approach of a CTD that is identifiable for 17.5 days; this CTD influences one additional jet streak. In contrast, the northwesterly flow jet streak intensifies in the absence of a CTD; the evolution in this case exposes the role of Rossby wave dynamics. The southwesterly flow jet streak is associated with a CTD that is tracked for 11.5 days and that participates in the intensification of one additional jet streak; the evolution in this hybrid case involves both a CTD and Rossby wave dynamics.

a. Trough-over-ridge jet streak

Figure 9a shows the position of the p_{trop} maximum for the CTD associated with the trough-over-ridge jet streak at 12-h intervals over its 17.5-day lifetime, and

Fig. 9b presents time series of the central values of p_{trop} and θ_{trop} associated with the CTD; a detailed history of the CTD is given in Table 1. The trajectory of the CTD is characterized by relatively slow, irregular movement at higher latitudes, and more rapid zonal movement while in proximity to the midlatitude jet stream (not shown). The CTD gradually strengthens between 0000 UTC 25 November and 0000 UTC 30 November 1991 as indicated by increasing values of p_{trop} and by decreasing values of θ_{trop} (Fig. 9b and Table 1).[2] Strengthening of the CTD during this time period also is indicated by an increase in the number of closed potential temperature contours (Table 1), signifying a greater degree of parcel trapping by the CTD. After maintaining quasi-steady behavior between 1200 UTC 30 November and 0000 UTC 3 December, the CTD undergoes dramatic weakening beginning at 1200 UTC 3 December as it fractures over the North Atlantic (not shown) while progressing equatorward (Fig. 9a); weakening of the CTD is indicated by an upward retreat of the DT and by an increase in the minimum value of θ_{trop} (Fig. 9b and Table 1). The rate of weakening slows by 0000 UTC 6 December, after which the CTD dissipates slowly while being swept eastward by the midlatitude jet stream until its demise at 1200 UTC 12 December over western China (Fig. 9a).

We now consider the evolution of the two jet streaks influenced by the CTD during its lifetime: the trough-over-ridge jet streak and an additional jet streak located upstream, referred to as the northerly flow jet streak. At 0000 UTC 30 November, the CTD is at peak intensity and is slowly moving equatorward from high latitudes (Table 1 and Fig. 9a). The CTD exhibits well-defined extrema of θ_{trop} (Fig. 10a) and p_{trop} (Fig. 10b), and is near the southwestern edge of an elongated cutoff cyclone in the 300-hPa geopotential height field (Fig. 10c). The 300-hPa wind speed pattern (Fig. 10c) shows an anticyclonically curved jet stream, with winds in excess of 50 m s^{-1}, in a region of large geopotential height gradient wrapping around a ridge off the west coast of North America. This jet stream also coincides with regions of large θ_{trop} and p_{trop} gradients (Figs. 10a,b), and PV gradients over the 316–324-K layer (Fig. 10d). The incipient northerly flow jet streak is discernible as a small wind speed maximum at 300 hPa (Fig. 10c) and as a local maximum in the PV gradient over the 316–324-K layer (Fig. 10d) located over northern British Columbia downstream from the crest of the ridge off the West Coast. The PV maximum associated with the CTD (Fig. 10d) is situated to the southwest of the p_{trop} maximum (denoted by an asterisk), indicating that in the lower stratosphere the core of the CTD tilts upward and equatorward toward the periphery of the polar vortex on the 320-K surface.

At 0000 UTC 1 December, the CTD is situated on the CS side of the northerly flow jet streak on the DT (Figs. 11a,b). This jet streak not only is well defined on the DT, but also on the 300-hPa (Fig. 11c) and 320-K (Fig. 11d) surfaces. The northerly flow jet streak has developed between 0000 UTC 30 November and 0000 UTC 1 December in conjunction with a decrease in the distance between the CTD and the periphery of the polar

TABLE 1. Summary information for the CTD associated with the trough-over-ridge jet streak at 12-h intervals from 0000 UTC 25 Nov to 1200 UTC 12 Dec 1991. For each 12-h analysis time the following are listed: the latitude and longitude (negative values denote °W) of the p_{trop} maximum associated with the CTD rounded to the nearest whole degree, the maximum value of p_{trop} and the minimum value of θ_{trop}, the speed of the CTD, and the number of closed θ_{trop} contours (contour interval, 6 K) associated with the CTD. The speed of the CTD is calculated using 6-h centered time differences based on positions at intermediate times (0600 and 1800 UTC; not shown); distances used in the calculation are determined from a great-circle formula (Steers 1970, section 8.6d). Note that the p_{trop} maximum and θ_{trop} minimum are not necessarily coincident, and that more precise values of latitude and longitude than indicated are used to determine great-circle distances.

Time and date	Lat (°N)	Lon (°)	p_{trop} (hPa)	θ_{trop} (K)	Speed (m s^{-1})	θ contours
0000 UTC 25 Nov	83	−49	459	279	—	0
1200 UTC 25 Nov	82	−48	501	276	0.4	0
0000 UTC 26 Nov	81	−55	507	274	5.2	1
1200 UTC 26 Nov	82	−77	514	274	8.8	1
0000 UTC 27 Nov	80	−91	592	272	6.8	2
1200 UTC 27 Nov	77	−100	637	268	10.4	3
0000 UTC 28 Nov	73	−92	666	264	9.0	3
1200 UTC 28 Nov	74	−87	666	265	2.6	2
0000 UTC 29 Nov	73	−91	658	264	5.3	2
1200 UTC 29 Nov	70	−98	701	262	8.1	3
0000 UTC 30 Nov	69	−97	826	252	3.2	5
1200 UTC 30 Nov	64	−103	657	263	18.2	4
0000 UTC 1 Dec	59	−105	669	262	12.9	4
1200 UTC 1 Dec	52	−98	683	263	21.8	3
0000 UTC 2 Dec	49	−86	679	264	24.8	3
1200 UTC 2 Dec	51	−71	682	268	21.5	3
0000 UTC 3 Dec	49	−60	703	268	29.9	4
1200 UTC 3 Dec	46	−42	762	276	18.5	2
0000 UTC 4 Dec	45	−34	656	291	13.9	2
1200 UTC 4 Dec	42	−30	522	296	8.6	1
0000 UTC 5 Dec	38	−29	575	302	18.5	0
1200 UTC 5 Dec	28	−26	486	309	23.5	2
0000 UTC 6 Dec	30	−17	410	313	24.0	1
1200 UTC 6 Dec	33	−20	401	314	6.6	1
0000 UTC 7 Dec	30	−20	392	317	7.8	0
1200 UTC 7 Dec	31	−19	384	318	2.6	1
0000 UTC 8 Dec	28	−18	395	318	7.2	1
1200 UTC 8 Dec	28	−16	398	318	6.0	0
0000 UTC 9 Dec	27	−12	405	320	17.2	1
1200 UTC 9 Dec	28	−4	376	319	19.7	0
0000 UTC 10 Dec	28	6	374	318	27.1	0
1200 UTC 10 Dec	30	21	384	316	41.0	0
0000 UTC 11 Dec	36	41	295	315	37.0	0
1200 UTC 11 Dec	37	53	271	318	24.9	0
0000 UTC 12 Dec	38	69	272	317	32.4	0
1200 UTC 12 Dec	38	84	244	320	—	0

[2] Changes in the minimum value of θ_{trop} associated with the CTD are hypothesized to be a manifestation of the nonconservation of potential temperature due to diabatic processes, and of PV (which affects the altitude of the DT) due to diabatic and frictional processes. Further consideration of the nonconservation of θ_{trop} would require detailed diagnostic analysis that is beyond the scope of this study.

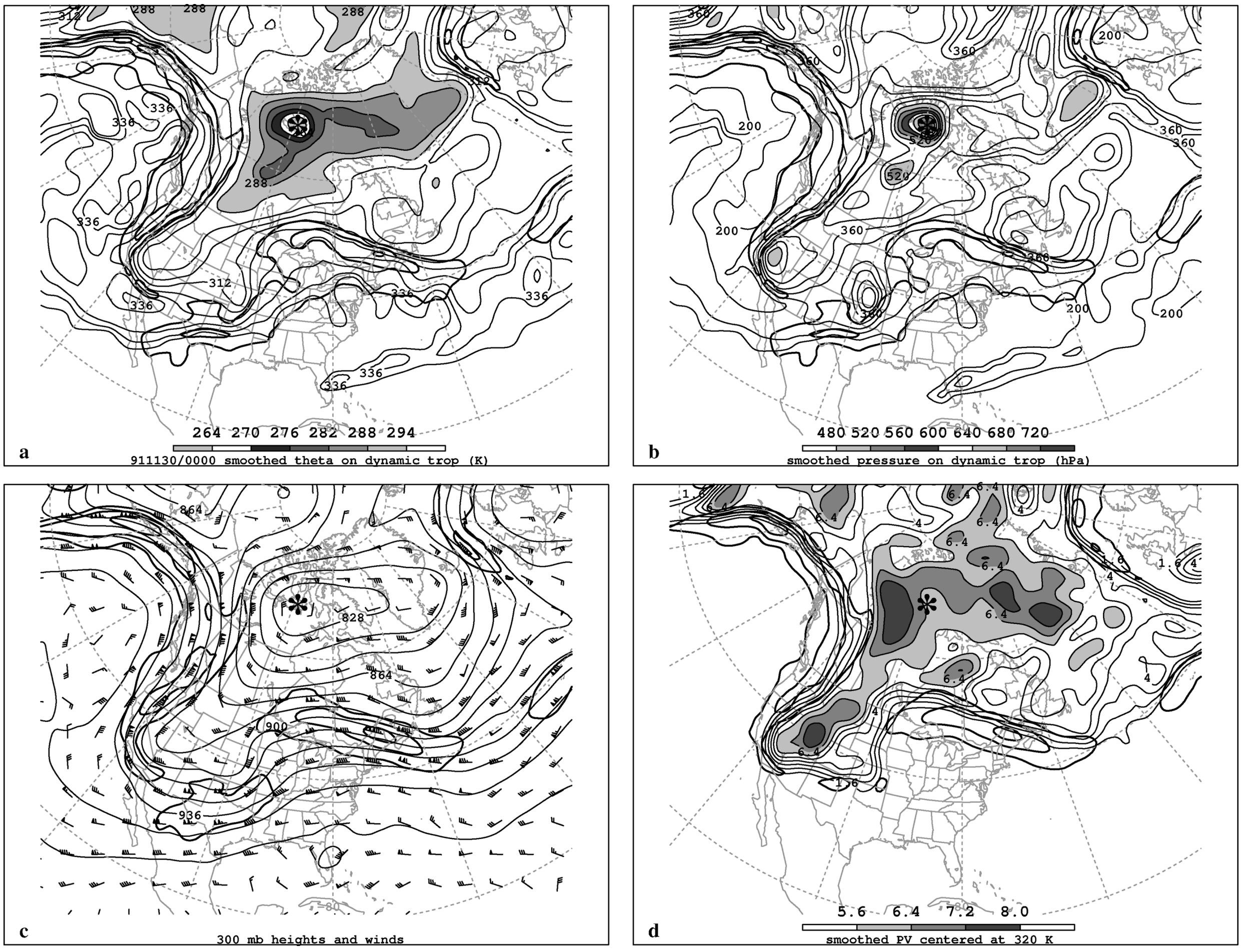

FIG. 10. Analyses for 0000 UTC 30 Nov 1991: (a) θ_{trop} (thin solid, values at and below 342 K contoured at a 6-K interval, shaded as indicated for values below 294 K) and horizontal wind speed on the DT (thick solid; contour interval, 15 m s^{-1}; starting at 50 m s^{-1}); (b) p_{trop} (thin solid; contour interval, 40 hPa; shaded as indicated for values greater than 480 hPa) and horizontal wind speed on the DT [contoured as in (a)]; (c) 300-hPa geopotential height (thin solid; contour interval, 12 dam), horizontal wind speed [contoured as in (a)], and horizontal winds (plotted at every third grid point using standard convention as specified in Fig. 1b); and (d) PV calculated over the 316–324-K layer (thin solid; contour interval 0.8 PVU for values greater than 1.6 PVU, shaded as indicated for values greater than 5.6 PVU) and horizontal wind speed at 320 K [contoured as in (a)]. A five-point smoother is applied to the θ_{trop}, p_{trop}, and PV fields. The position of the p_{trop} maximum associated with the CTD of interest is marked with an asterisk in each panel.

vortex, resulting in increased gradients of θ_{trop} and p_{trop}, geopotential height at 300 hPa, and PV over the 316–324-K layer (cf. Figs. 10a–d and 11a–d). A broad jet streak is apparent in the southwesterly flow extending downstream from a 300-hPa trough axis located over the southwestern United States (Fig. 11c); this feature corresponds to the trough-over-ridge jet streak. The trough-over-ridge jet streak intensifies between 0000 UTC 30 November and 0000 UTC 1 December as the major axis of the 300-hPa cutoff cyclone rotates cyclonically and comes into phase with a weak short-wave trough emerging from the southern plains during this 24-h period (Figs. 10c and 11c). This reconfiguration of the cutoff cyclone also is apparent on the DT in the evolution of the 294-K potential temperature contour between 0000 UTC 30 November and 0000 UTC 1 December (Figs. 10a and 11a).

During the 36-h period ending at 1200 UTC 2 December, the time of kinematic interest for this case, the CTD shifts to the eastern side of the 300-hPa trough, and the cutoff cyclone changes its orientation from approximately northeast–southwest to northwest–southeast (cf. Figs. 11c and 12c). The CTD has come into close proximity to the trough-over-ridge jet streak, and is located on the CS side and slightly downstream from the jet core at 300 hPa and at 320 K (Figs. 12c,d). Consistent with the location of the CTD relative to this jet streak, the θ_{trop} minimum (Fig. 12a) is found on the CS side and is displaced slightly downstream from the core; the location of the θ_{trop} minimum closely matches those of the 300-hPa temperature maximum (Fig. 1b) and 500-hPa temperature minimum (Fig. 1d) discussed in section 3a. This thermal structure, along with the localized p_{trop} maximum (Fig. 12b), is a signature of the

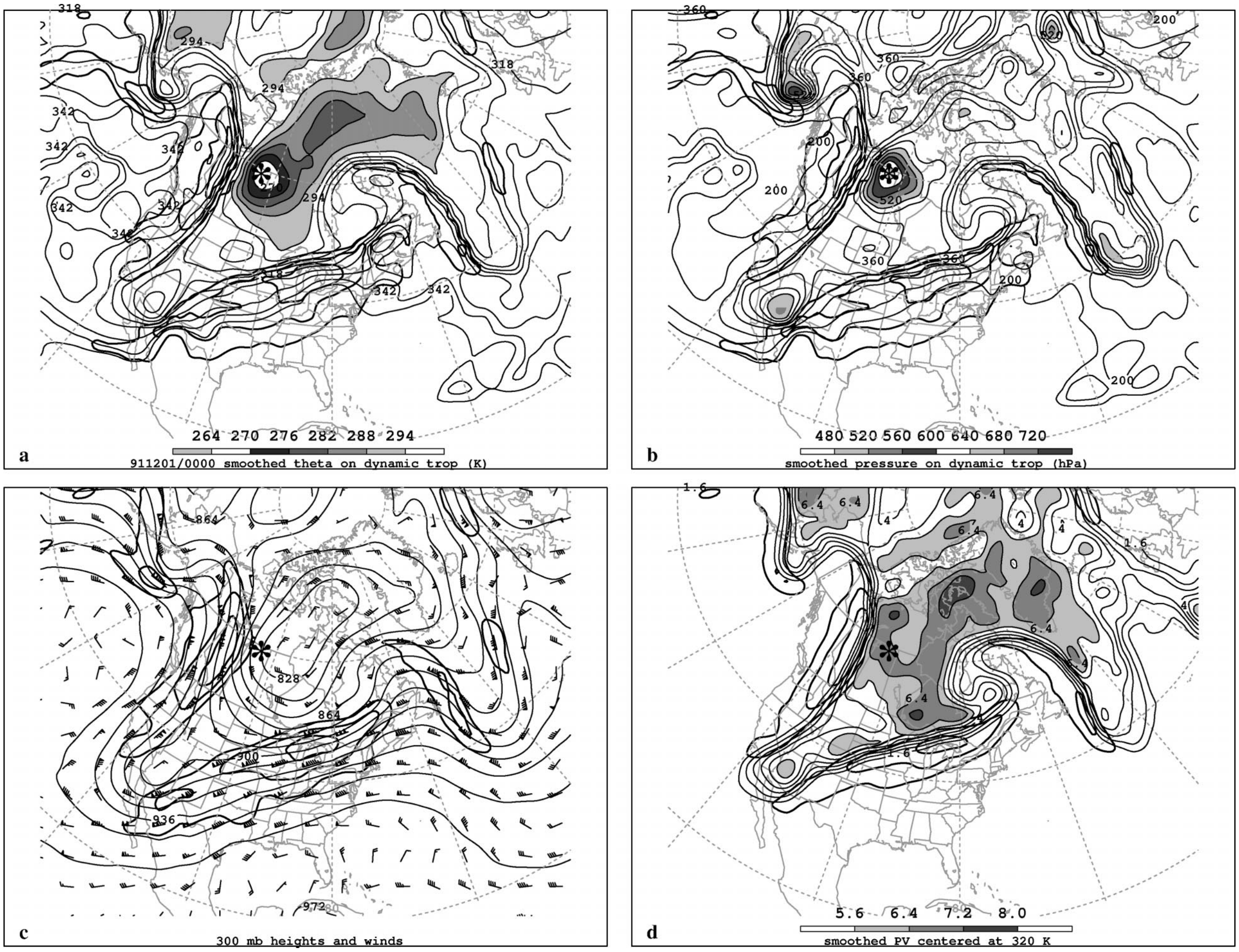

FIG. 11. As in Fig. 10 except at 0000 UTC 1 Dec 1991.

downward penetration of stratospheric air into the troposphere in the form of a tropopause fold (not shown) beneath the trough-over-ridge jet streak. The CTD also has elongated in the along-flow direction (Figs. 12a,b), quite likely in response to the strong cyclonic shear found along its equatorward edge.

In conjunction with the above evolution between 0000 UTC 1 December and 1200 UTC 2 December, the northerly flow jet streak weakens and the broad trough-over-ridge jet streak strengthens on the 300-hPa surface (cf. Figs. 11c and 12c) and on the DT (cf. Figs. 11a,b and 12a,b). For subsequent comparison in section 4c, the trough-over-ridge jet streak strengthens from 91 to 104 m s^{-1} on the DT with the approach of the CTD; most of this increase (11 out of 13 m s^{-1}) occurs over the first 12 h of this 36-h period. Although weakening of the northerly flow jet streak also is evident on the 320-K surface during this same time period, concomitant strengthening of the trough-over-ridge jet streak does not occur on this isentropic surface; this discrepancy is related to the positioning of the 320-K surface below the level of maximum wind for the latter jet streak (i.e., 332 K) at 1200 UTC 2 December.

By 0000 UTC 4 December, the CTD has elongated farther along the direction of the trough-over-ridge jet streak (Figs. 13a,b) and has moved toward the downstream edge of this feature, which has extended around a low-amplitude ridge at 300 hPa (Fig. 13c). The CTD exhibits a double structure in the p_{trop} field (Fig. 13b) at 0000 UTC 4 December, having fractured 12 h earlier. It is of interest in regard to the selection of p_{trop} as the primary tracking variable (section 2b) that this double structure is evident only in the p_{trop} field, and not in the θ_{trop} (Fig. 13a) or in the 316–324-K PV (Fig. 13d) fields. The CTD is identified with the downstream member of the double maximum in p_{trop}, which heads equatorward while the upstream member drifts poleward. Although either or both members could be tracked following fracture of the original CTD, the rationale for identifying the CTD with the equatorward-moving p_{trop} maximum is that this alternative provides better continuity in the track and in the temporal evolution of the extrema of θ_{trop} and p_{trop} during the remainder of the lifetime of the CTD.

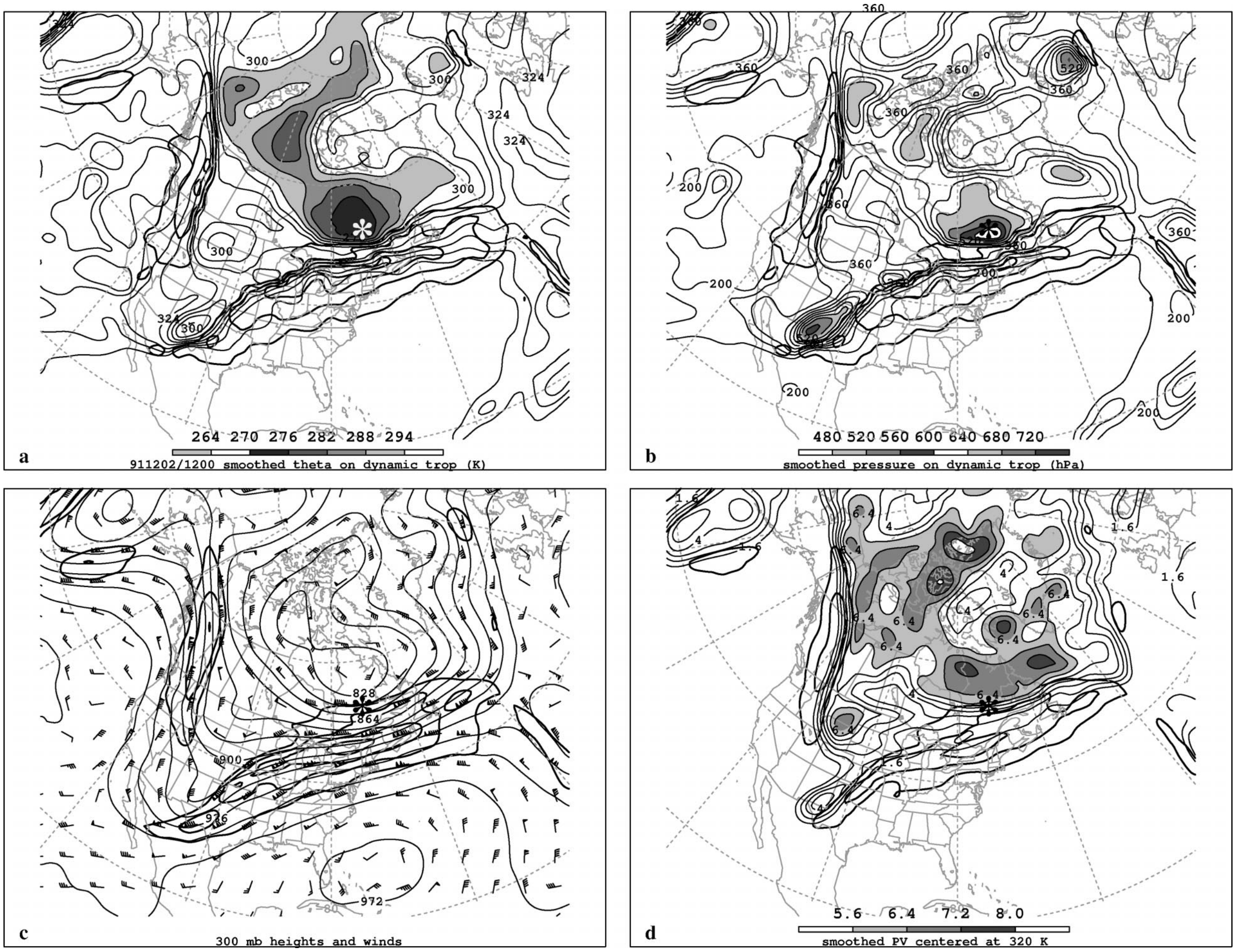

FIG. 12. As in Fig. 10 except at 1200 UTC 2 Dec 1991.

b. Northwesterly flow jet streak

At 0000 UTC 9 November 1995, 48 h before the time of kinematic interest for the northwesterly flow case, the nascent jet streak is located over the eastern North Pacific and features wind speeds on the DT exceeding 60 m s^{-1} (Fig. 14a). This jet streak is developing in a confluence zone found downstream from a meridionally oriented ridge-over-trough pattern located over the central North Pacific. (The confluence zone and ridge-over-trough pattern are depicted in terms of the 300-hPa geopotential height field in Fig. 14a and subsequent panels.) This pattern results from the zonal juxtaposition of a quasi-stationary high-latitude ridge with a narrow, mobile trough that is part of the Rossby wave train constituting the midlatitude westerlies. At 0000 UTC 9 November (Fig. 14a), the high-latitude ridge is manifested on the DT as a p_{trop} minimum centered over the northwestern coast of Alaska, whereas the midlatitude trough is manifested on the DT as a meridionally elongated p_{trop} maximum. The confluence zone in which the jet streak is developing corresponds to the large horizontal gradient of p_{trop} located over the eastern North Pacific between higher and lower values of p_{trop} situated poleward and equatorward of the jet streak, respectively.

During the next 12 h, the nascent northwesterly flow jet streak strengthens significantly on the DT, with maximum wind speeds increasing to greater than 80 m s^{-1} by 1200 UTC 9 November (Fig. 14b). Strengthening of the jet streak occurs in concert with the fracture and poleward retraction of the central North Pacific trough such that the meridional separation between the base of the trough and the crest of the ridge decreases. This decrease in meridional scale is associated with an increase in the horizontal gradient of p_{trop} in the downstream confluence zone and with intensification of the jet streak. Between 0000 UTC 10 November (Fig. 14c) and 0000 UTC 11 November (Fig. 14d), the northwesterly flow jet streak becomes more compact in the along-stream direction and the wind speed maximum consolidates into a single feature. This evolution occurs as the confluence zone rotates anticyclonically and moves eastward into western North America in conjunction with the amplification of an upstream ridge and downstream trough in the midlatitude westerlies.

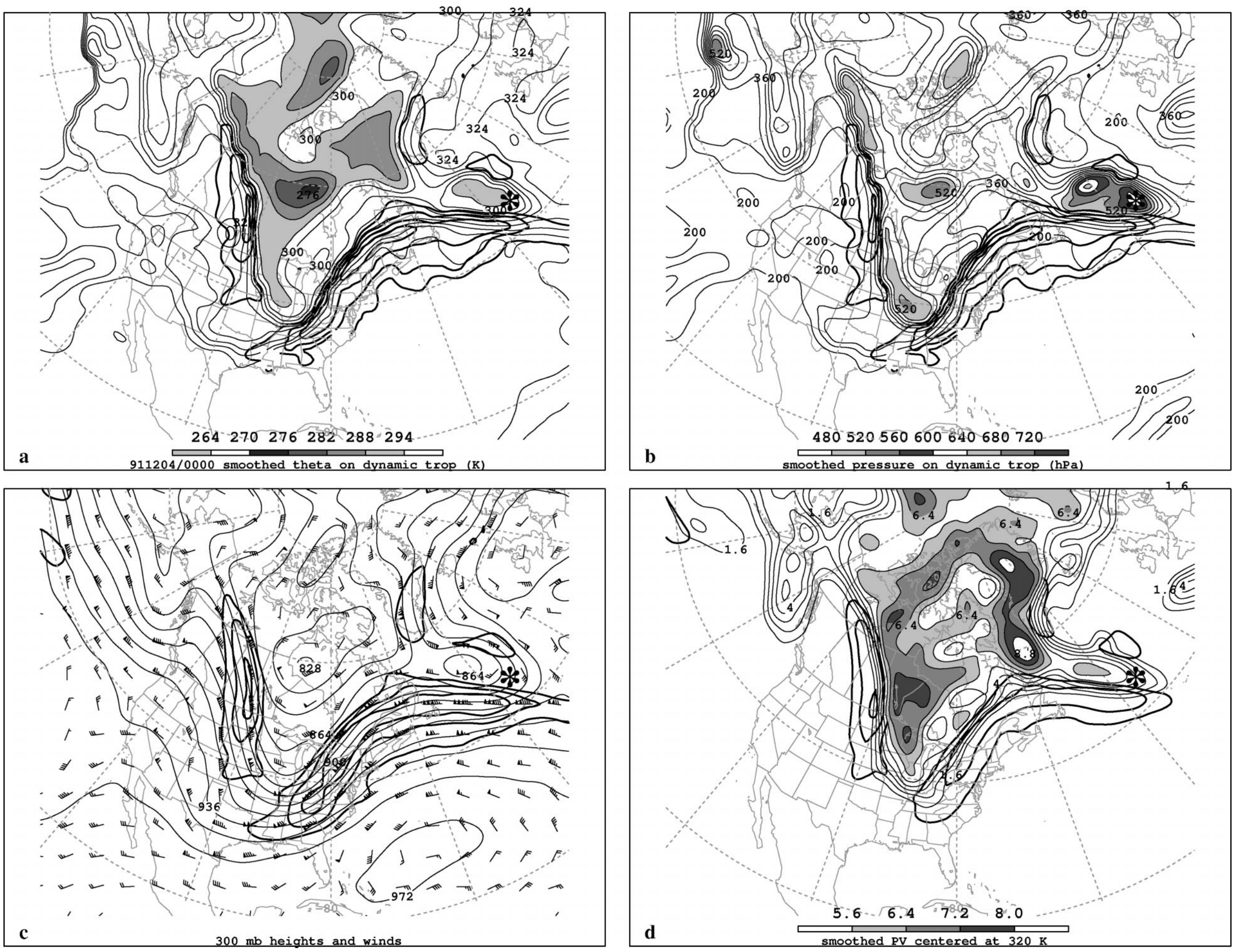

FIG. 13. As in Fig. 10 except at 0000 UTC 4 Dec 1991.

c. Southwesterly flow jet streak

The CTD associated with the southwesterly flow jet streak is tracked over the 11.5-day period between 0000 UTC 18 October and 1200 UTC 29 October 1995, which brackets the time of kinematic interest (0000 UTC 28 October) for this case. This CTD also is associated with the intensification of a separate jet streak over the western North Pacific between 0000 UTC 22 October and 1200 UTC 22 October, the evolution of which is illustrated beginning at 0000 UTC 21 October (Fig. 15a). At this time, a jet streak extends off the coast of Japan, bounded on its poleward side by an intense, localized p_{trop} maximum (thus qualifying as a CTD), while the CTD that eventually will influence the southwesterly flow jet streak is moving across the east coast of Russia. At 1200 UTC 21 October (Fig. 15b), the jet streak weakens slightly as the initial p_{trop} maximum pivots away from it, while the CTD approaches from the northwest.

During the next 12 h, the initial p_{trop} maximum continues moving away from the jet streak while the CTD continues moving toward it; the region of wind speed exceeding 40 m s^{-1} on the DT expands poleward toward the approaching CTD and extends westward toward a p_{trop} maximum that is crossing Japan (Fig. 15c). At 1200 UTC 22 October (Fig. 15d), this p_{trop} maximum remains positioned in the jet-entrance region, while the CTD comes into sufficiently close proximity to the jet streak to have a dramatic influence: the maximum wind speed on the DT has increased from 67 to 92 m s^{-1} during the preceding 12-h period, accompanied by a significant increase in the p_{trop} gradient across the jet streak (Figs. 15c,d). As in the trough-over-ridge case, the close approach of a CTD to a preexisting jet feature coincides with an increase in jet-streak wind speeds; the increase in the present case of 25 m s^{-1}, which is confined to a 12-h period, is nearly twice that in the former case, which occurs over a 36-h period (see section 4a).

We now consider the evolution culminating in the formation of the southwesterly flow jet streak. After traversing the North Pacific, the CTD and the associated jet streak previously considered at 1200 UTC 22 October (Fig. 15d) are located over the northern Rockies and off the coast of British Columbia, respectively, at 1200 UTC 26 October (Fig. 16a); both features are

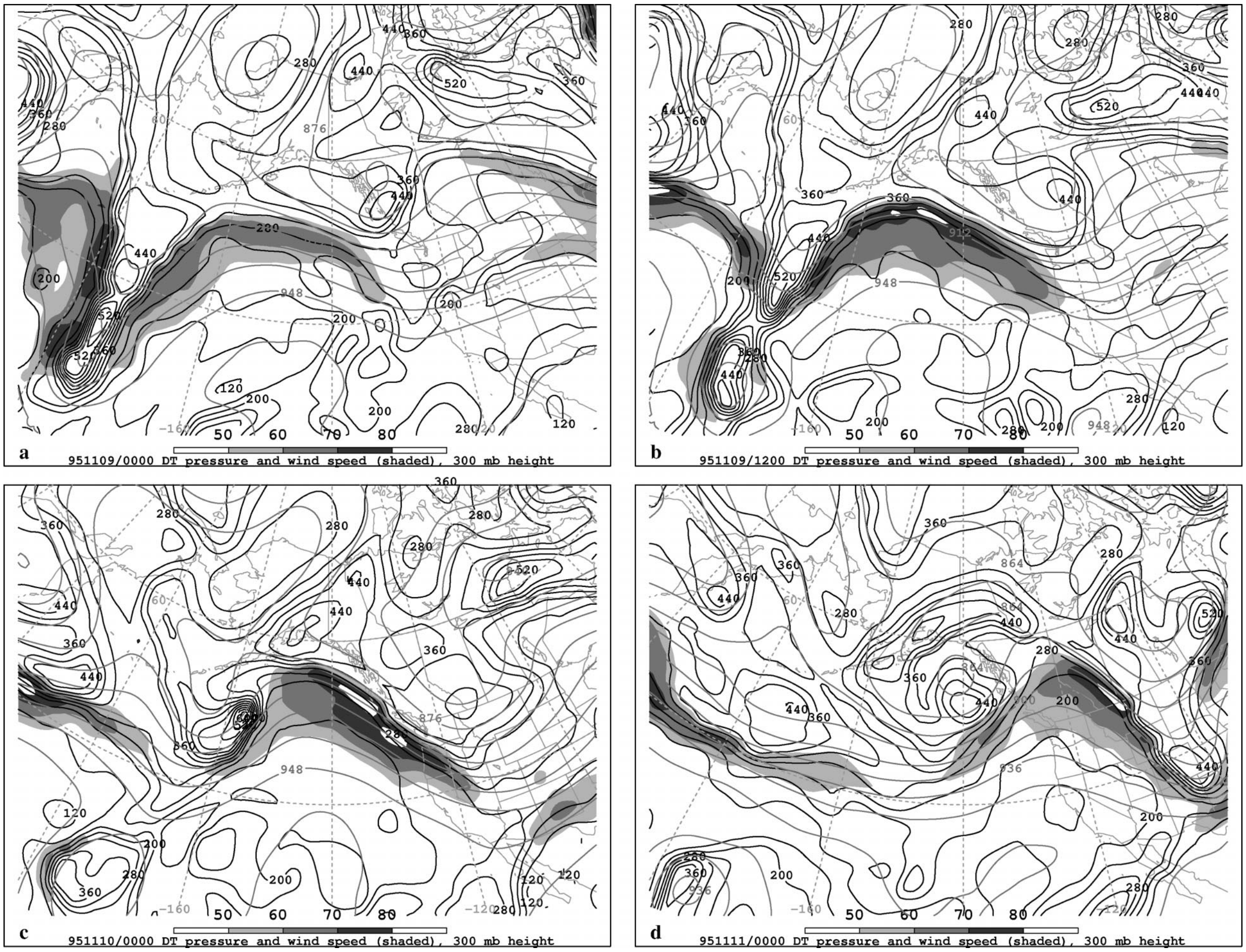

FIG. 14. Analyses of p_{trop} (black solid; contour interval, 40 hPa), horizontal wind speed on the DT (shaded as indicated for values greater than 50 m s^{-1}), and 300-hPa geopotential height (gray solid; contour interval, 12 dam) at (a) 0000 UTC 9 Nov, (b) 1200 UTC 9 Nov, (c) 0000 UTC 10 Nov, and (d) 0000 UTC 11 Nov 1995. A five-point smoother is applied to the p_{trop} field.

found in northwesterly flow upstream from an upper-level trough at 300 hPa. The location of the CTD corresponds to the downstream edge of a band of large p_{trop} gradient and to the exit region of the northwesterly flow jet streak. By 0000 UTC 27 October (Fig. 16b), the CTD has weakened and elongated in the along-flow direction, while remaining at the downstream edge of the strong p_{trop} gradient.

The southwesterly flow jet streak emerges at 1200 UTC 27 October (Fig. 16c), as the CTD moves to the downstream side of the upper-level trough. By 0000 UTC 28 October (Fig. 16d), the southwesterly flow jet streak has become better defined while the northwesterly flow jet streak has weakened. A swath of large p_{trop} gradient now extends from the coast of British Columbia southeastward through the trough base and then northeastward toward the CTD, which is centered over southeastern Ontario. The weakening of the upstream (i.e., northwesterly flow) jet streak, and the formation and strengthening of the downstream (i.e., southwesterly flow) jet streak, evident between 1200 UTC 27 October and 0000 UTC 28 October (Figs. 16c,d), is suggestive of downstream baroclinic development (recall the discussion in section 1) in the following sense: there is a weakening EKE maximum upstream from a trough axis (here a jet-streak wind speed maximum is taken to be a proxy for an EKE maximum) and a strengthening EKE maximum downstream (see, e.g., Orlanski and Sheldon 1995, Fig. 3). The present evolution differs from classic downstream development, however, through the addition of a CTD to EKE dispersion in the formation of the downstream jet streak.

5. Summary and future directions

A diagnostic study has been presented of the kinematics and evolution of three upper-level jet streaks over North America. These jet streaks were selected to represent the three (out of four) phases of the Shapiro (1982) conceptual model of the progression of a jet streak through a synoptic-scale baroclinic wave where jet streaks are relatively straight: trough-over-ridge

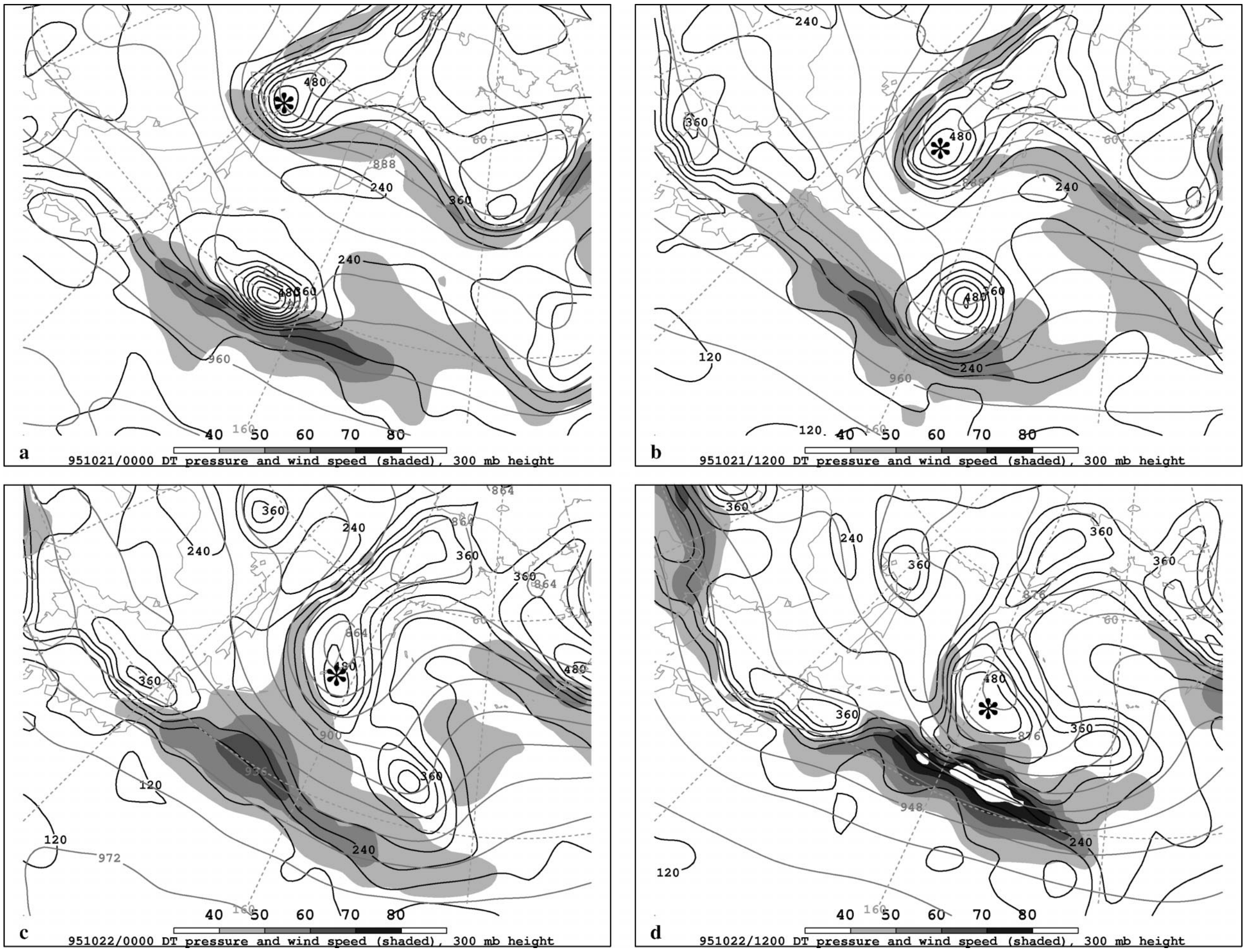

FIG. 15. Analyses of p_{trop} (black solid; contour interval, 40 hPa), horizontal wind speed on the DT (shaded as indicated for values greater than 40 m s^{-1}), and 300-hPa geopotential height (gray solid; contour interval, 12 dam) at (a) 0000 UTC 21 Oct, (b) 1200 UTC 21 Oct, (c) 0000 UTC 22 Oct, and (d) 1200 UTC 22 Oct 1995. The position of the p_{trop} maximum associated with the CTD of interest is marked with an asterisk in each panel, and a five-point smoother is applied to the p_{trop} field.

(1200 UTC 2 December 1991), northwesterly flow (0000 UTC 11 November 1995), and southwesterly flow (0000 UTC 28 October 1995). Although kinematic signatures consistent with the classic four-quadrant conceptual model for a straight jet streak are diagnosed, flow curvature, thermal advection, and the position of the jet streak within the synoptic-scale flow pattern are found to contribute to departures from this basic conceptual model. The latter factor, which is prominent in the northwesterly and southwesterly flow jet streaks, reflects the influence of neighboring short-wave features in the synoptic-scale flow pattern on the kinematic fields associated with a particular jet streak.

A kinematic signature common to all three cases is ageostrophic flow directed toward lower (higher) geopotential heights in the jet-entrance (-exit) region, as anticipated from the straight jet-streak conceptual model. Despite differences in detail between the three cases, a Helmholtz decomposition of the ageostrophic wind yields a rotational ageostrophic wind pattern consisting of cyclonic gyres centered upstream from the entrance region and downstream from the exit region; this pattern is sufficient to explain the cross-contour ageostrophic flow diagnosed in the jet-entrance and -exit regions. The divergent ageostrophic wind either is comparable to or weaker than the rotational part, but contributes in the same sense as the rotational part to cross-contour ageostrophic flow within the entrance and exit regions. These signatures in the ageostrophic wind are best defined in the trough-over-ridge jet streak, which is the most isolated of the three jet streaks considered in this study.

The well-defined ageostrophic wind signatures and their agreement with the straight jet-streak conceptual model in the trough-over-ridge case motivate further assessment of this conceptual model in terms of the midtropospheric vertical motion (ω) field for this case. In this assessment, the kinematic ω is compared with the QG ω, diagnosed using an adiabatic version of the QG ω equation with the forcing expressed in terms of the Q vector. The QG ω field also is separated into

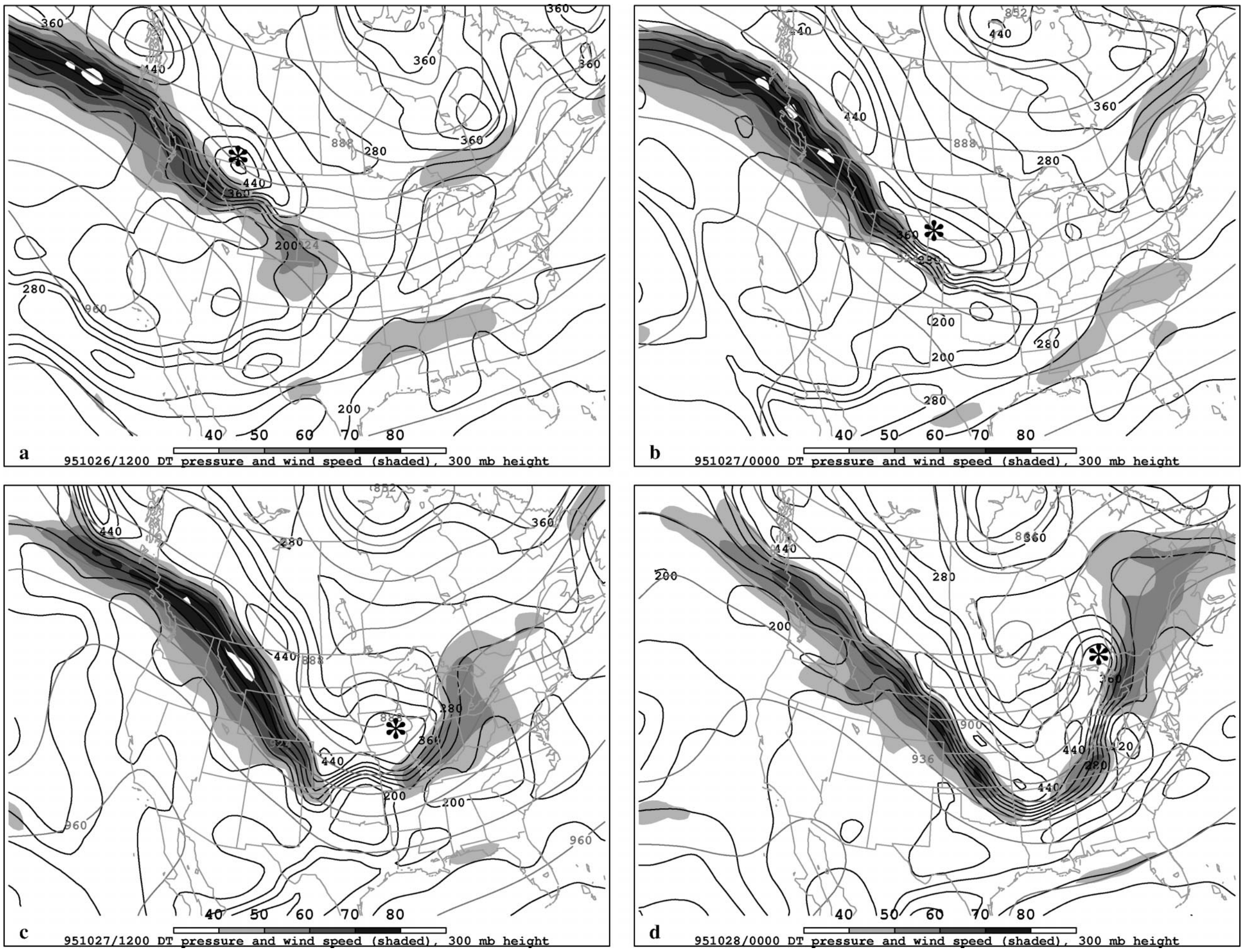

FIG. 16. As in Fig. 15 except at (a) 1200 UTC 26 Oct, (b) 0000 UTC 27 Oct, (c) 1200 UTC 27 Oct, and (d) 0000 UTC 28 Oct 1995.

components associated with flow curvature (ω_s) and with parcel accelerations into and out of a jet streak (ω_n), the latter signified by confluence in the entrance region and diffluence in the exit region. Despite the relatively straight and isolated nature of the trough-over-ridge jet streak, a four-cell pattern is not evident in the kinematic ω nor in the QG ω fields, which feature a two-cell pattern composed of subsidence and ascent upstream and downstream from the jet core, respectively. This signature is reproduced in the ω_s field, consistent with the presence of cyclonic streamline curvature on the poleward [i.e., cyclonic shear (CS)] side of the jet streak. The ω_n field contains an asymmetric four-cell pattern, with larger magnitudes featured on the CS side of the jet streak; aside from this asymmetry, the diagnosed four-cell pattern is consistent with the straight jet-streak conceptual model. Nevertheless, the dominance of $|\omega_s|$ over $|\omega_n|$ suggests that cyclonic curvature poleward of the jet streak has a stronger influence on the QG vertical motion than parcel accelerations in the entrance and exit regions, accounting for the two-cell pattern in total QG ω on the CS side of the jet streak.

Cross sections of the divergent ageostrophic circulation, taken along the axis and across the entrance and exit regions of the trough-over-ridge jet streak, provide an additional means to evaluate the straight jet-streak conceptual model. The projection of the divergent ageostrophic circulation onto the cross-section plane tangent to the axis of the jet streak indicates descent and ascent behind and ahead of the jet streak, respectively, consistent with the two-cell pattern in the midtropospheric vertical motion field discussed above. Thermodynamically direct and indirect patterns are evident in the projections of the divergent ageostrophic circulations onto cross sections normal to the jet-entrance and -exit regions, respectively, in accord with the straight jet-streak conceptual model. The projection of the divergent ageostrophic circulation onto the cross-section plane normal to the exit region further reveals an indirect circulation shifted significantly toward the equatorward (i.e., anticyclonic shear) side of the jet core. This shift is consistent with the conceptual model of Shapiro (1982) for the case of warm advection in the exit region.

Refinements to the QG ω-equation methodology that would enable further reconciliation of observed vertical circulation patterns in the vicinity of jet–front systems with kinematic conceptual models are feasible given present knowledge. The natural coordinate partition of the Q vector proposed by Jusem and Atlas (1998), which isolates vertical motion patterns attributable to confluence/diffluence, flow curvature, and thermal advection, might portray the signatures described by the kinematic conceptual models more effectively than the two-component approach adopted in the present study. Diabatic processes, latent heating in particular, may be incorporated into the forcing for the QG ω equation, as their neglect is hypothesized to have contributed to underestimation of ascent in the trough-over-ridge and southwesterly flow jet streaks. An additional opportunity for improving the agreement between the diagnosed and analyzed vertical motion fields is afforded by generalized ω equations that account for spatially varying static stability, baroclinicity, and inertial stability in the elliptic operator, and that use a less restrictive balanced wind than geostrophic, such as the nondivergent wind, in the forcing term. A diagnostic equation for the divergent flow proposed by Eliassen (1984) and designed for application in baroclinic zones as an extension of the Sawyer–Eliassen frontal circulation equation to three dimensions is an attractive candidate, as is the so-called alternative balance ω equation proposed by Davies-Jones (1991).

Jet-streak evolution has been investigated in relation to coherent tropopause disturbances (CTDs) and Rossby waves, with a view toward examining the relative contributions of these respective features among the three cases documented in this study. A CTD contributes to the intensification of the trough-over-ridge jet streak; this CTD is identifiable for 17.5 days and influences not only the jet streak considered for kinematic study but also one additional jet streak. In contrast, the northwesterly flow jet streak intensifies in the absence of a CTD; the evolution in this case is characterized by Rossby wave dynamics. The southwesterly flow jet streak is associated with a CTD that is tracked for 11.5 days and that participates in the intensification of one additional jet streak; the evolution in this hybrid case involves both a CTD and Rossby wave dynamics. Irrespective of the involvement of a CTD, in all three cases the jet streaks coincide with large horizontal gradients of p_{trop} and θ_{trop}, and of PV on tropopause-intersecting isentropic surfaces. In the two cases involving CTDs, their role is to enhance these respective gradients over a mesoscale region, which appears to focus and strengthen jet-streak winds over the same region. This enhancement requires the close approach of a CTD to the background jet stream or to a preexisting jet streak; the episodic nature of this process offers a possible explanation for the observed transient behavior of jet streaks in the context of balanced dynamics, and provides a complementary interpretation to downstream baroclinic development for the discontinuous nature of the motion of jet streaks through a Rossby wave train.

The participation of the respective CTDs in the trough-over-ridge and southwesterly flow cases in the evolution of an additional jet streak in each case, along with the documented longevity of these CTDs, suggests that an individual CTD may be involved in the formation or intensification of multiple jet streaks during its lifetime. This suggestion points toward the opportunity to conduct observational studies of the life cycles of CTDs, which may be addressed from climatological and case study perspectives, and which would complement and extend existing climatologies of upper-level short-wave troughs (e.g., Sanders 1988; Lefevre and Nielsen-Gammon 1995; Dean and Bosart 1996). A related topic concerns the origin of CTDs, which appears to be favored in high-latitude regions far from the disruptive influence of strong shearing associated with the polar-front jet stream. The timescales of CTD genesis and the documented lifetimes of up to several weeks may be sufficiently long to require consideration of radiative, in addition to dynamical, processes.

The present qualitative treatment of CTDs and their influence on jet streaks points toward the opportunity to quantify the influence of CTDs on jet-streak evolution in observed cases. Piecewise PV-inversion methodologies (e.g., Davis and Emanuel 1991; Davis 1992; Hakim et al. 1996) provide a diagnostic framework for attributing the balanced wind field to the respective PV gradients associated with CTDs and with the Rossby waveguide corresponding to the equatorward boundary of the planetary-scale polar vortex. Potential vorticity inversion and attribution would allow the role of jet streaks in the dynamics of extratropical flows to be reinterpreted in terms of interactions between CTDs and Rossby waves; candidate opportunities for investigation include the roles of CTDs in cyclogenesis and in downstream baroclinic development. An additional topic of contemporary interest concerns the role of CTDs in the predictability of extratropical flows. CTDs are hypothesized to be important from a predictability standpoint because the characteristic mesoscale structure of these features potentially compromises their analysis, particularly in data-sparse oceanic and arctic regions. Consequently, the predictability of extratropical weather events may be limited in circumstances favoring interactions between CTDs and midlatitude Rossby waves, such as planetary-scale flow regimes exhibiting high-amplitude ridges over western North America that correspond to the positive phase of the Pacific–North American (PNA) pattern.

Acknowledgments. We thank Mr. A. Loughe, and Drs. D. Knight, G. Lackmann, and C.-C. Lai for their efforts in developing and improving the SUNYPAK diagnostic software, and the two anonymous reviewers for their recommendations and advice on improving the presentation of this paper. The first author also thanks Drs. P.

Cunningham and G. Hakim for fruitful discussions on jet-streak evolution and dynamics. Financial support for this research was provided by a University at Albany Presidential Fellowship awarded to the first author, and by the National Science Foundation through Grants ATM-9421678 and ATM-9818088, awarded to the University at Albany, State University of New York.

REFERENCES

Barnes, S. L., and B. R. Colman, 1993: Quasigeostrophic diagnosis of cyclogenesis associated with a cutoff extratropical cyclone—The Christmas 1987 storm. *Mon. Wea. Rev.,* **121,** 1613–1634.

——, and ——, 1994: Diagnosing an operational numerical model using *Q*-vector and potential vorticity concepts. *Wea. Forecasting,* **9,** 85–102.

Beebe, R. G., and F. C. Bates, 1955: A mechanism for assisting in the release of convective instability. *Mon. Wea. Rev.,* **83,** 1–10.

Bjerknes, J., 1951: Extratropical cyclones. *Compendium of Meteorology,* T. F. Malone, Ed., Amer. Meteor. Soc., 577–598.

——, and J. Holmboe, 1944: On the theory of cyclones. *J. Meteor.,* **1,** 1–22.

Bluestein, H. B., 1993: *Observations and Theory of Weather Systems.* Vol. II, *Synoptic–Dynamic Meteorology in Midlatitudes,* Oxford University Press, 594 pp.

——, and K. W. Thomas, 1984: Diagnosis of a jet streak in the vicinity of a severe weather outbreak in the Texas panhandle. *Mon. Wea. Rev.,* **112,** 2499–2520.

Bosart, L. F., G. J. Hakim, K. R. Tyle, M. A. Bedrick, W. E. Bracken, M. J. Dickinson, and D. M. Schultz, 1996: Large-scale antecedent conditions associated with the 12–14 March 1993 cyclone (''superstorm '93'') over eastern North America. *Mon. Wea. Rev.,* **124,** 1865–1891.

Brill, K. F., L. W. Uccellini, J. Manobianco, P. J. Kocin, and J. H. Homan, 1991: The use of successive dynamic initialization by nudging to simulate cyclogenesis during GALE IOP 1. *Meteor. Atmos. Phys.,* **45,** 15–40.

Cahir, J. J., 1971: Implications of circulations in the vicinity of jet streaks at subsynoptic scales. Ph.D. dissertation, The Pennsylvania State University, 170 pp. [Available from Dept. of Meteorology, The Pennsylvania State University, University Park, PA 16802.]

Cammas, J.-P., and D. Ramond, 1989: Analysis and diagnosis of the composition of ageostrophic circulations in jet-front systems. *Mon. Wea. Rev.,* **117,** 2447–2462.

Chen, S.-J., and L. Dell'Osso, 1987: A numerical case study of east Asian coastal cyclogenesis. *Mon. Wea. Rev.,* **115,** 477–487.

Cunningham, P., and D. Keyser, 2000: Analytical and numerical modelling of jet streaks: Barotropic dynamics. *Quart. J. Roy. Meteor. Soc.,* **126,** 3187–3217.

Davies, H. C., and A. M. Rossa, 1998: PV frontogenesis and upper-tropospheric fronts. *Mon. Wea. Rev.,* **126,** 1528–1539.

Davies-Jones, R., 1991: The frontogenetical forcing of secondary circulations. Part I: The duality and generalization of the Q vector. *J. Atmos. Sci.,* **48,** 497–509.

Davis, C. A., 1992: Piecewise potential vorticity inversion. *J. Atmos. Sci.,* **49,** 1397–1411.

——, and K. A. Emanuel, 1991: Potential vorticity diagnostics of cyclogenesis. *Mon. Wea. Rev.,* **119,** 1929–1953.

Dean, D. B., and L. F. Bosart, 1996: Northern Hemisphere 500-hPa trough merger and fracture: A climatology and case study. *Mon. Wea. Rev.,* **124,** 2644–2671.

desJardins, M. L., K. F. Brill, S. Jacobs, S. S. Schotz, and P. Bruehl, 1995: N-AWIPS user's guide. Version 5.2.1, NOAA/NWS/National Centers for Environmental Prediction, 302 pp. [Available from NOAA/NCEP, Rm. 100, WWBG, 5200 Auth Rd., Camp Springs, MD 20746.]

Donnadille, J., J.-P. Cammas, P. Mascart, and D. Lambert, 2001a: FASTEX IOP 18: A very deep tropopause fold. II: Quasi-geostrophic omega diagnoses. *Quart. J. Roy. Meteor. Soc.,* **127,** 2269–2286.

——, ——, ——, ——, and R. Gall, 2001b: FASTEX IOP 18: A very deep tropopause fold. I: Synoptic description and modelling. *Quart. J. Roy. Meteor. Soc.,* **127,** 2247–2268.

Eliassen, A., 1984: Geostrophy. *Quart. J. Roy. Meteor. Soc.,* **110,** 1–12.

Hakim, G. J., 2000: Climatology of coherent structures on the extratropical tropopause. *Mon. Wea. Rev.,* **128,** 385–406.

——, and L. W. Uccellini, 1992: Diagnosing coupled jet-streak circulations for a northern plains snow band from the operational nested-grid model. *Wea. Forecasting,* **7,** 26–48.

——, and D. Keyser, 2001: Canonical frontal circulation patterns in terms of Green's functions for the Sawyer–Eliassen equation. *Quart. J. Roy. Meteor. Soc.,* **127,** 1795–1814.

——, L. F. Bosart, and D. Keyser, 1995: The Ohio Valley wave-merger cyclogenesis event of 25–26 January 1978. Part I: Multiscale case study. *Mon. Wea. Rev.,* **123,** 2663–2692.

——, D. Keyser, and L. F. Bosart, 1996: The Ohio Valley wave-merger cyclogenesis event of 25–26 January 1978. Part II: Diagnosis using quasigeostrophic potential vorticity inversion. *Mon. Wea. Rev.,* **124,** 2176–2205.

Hoinka, K. P., 1998: Statistics of the global tropopause pressure. *Mon. Wea. Rev.,* **126,** 3303–3325.

Jusem, J. C., and R. Atlas, 1998: Diagnostic evaluation of vertical motion forcing mechanisms by using Q-vector partitioning. *Mon. Wea. Rev.,* **126,** 2166–2184.

Keyser, D., and M. A. Shapiro, 1986: A review of the structure and dynamics of upper-level frontal zones. *Mon. Wea. Rev.,* **114,** 452–499.

——, M. J. Reeder, and R. J. Reed, 1988: A generalization of Petterssen's frontogenesis function and its relation to the forcing of vertical motion. *Mon. Wea. Rev.,* **116,** 762–780.

——, B. D. Schmidt, and D. G. Duffy, 1989: A technique for representing three-dimensional vertical circulations in baroclinic disturbances. *Mon. Wea. Rev.,* **117,** 2463–2494.

——, B. D. Schmidt, and D. G. Duffy, 1992: Quasigeostrophic vertical motions diagnosed from along- and cross-isentrope components of the Q vector. *Mon. Wea. Rev.,* **120,** 731–741.

Keyser, D. A., and D. R. Johnson, 1984: Effects of diabatic heating on the ageostrophic circulation of an upper tropospheric jet streak. *Mon. Wea. Rev.,* **112,** 1709–1724.

Krishnamurti, T. N., 1968: A study of a developing wave cyclone. *Mon. Wea. Rev.,* **96,** 208–217.

Kurz, M., 1992: Synoptic diagnosis of frontogenetic and cyclogenetic processes. *Meteor. Atmos. Phys.,* **48,** 77–91.

Lackmann, G. M., D. Keyser, and L. F. Bosart, 1997: A characteristic life cycle of upper-tropospheric cyclogenetic precursors during the Experiment on Rapidly Intensifying Cyclones over the Atlantic (ERICA). *Mon. Wea. Rev.,* **125,** 2729–2758.

Lefevre, R. J., and J. W. Nielsen-Gammon, 1995: An objective climatology of mobile troughs in the Northern Hemisphere. *Tellus,* **47A,** 638–655.

Loughe, A. F., C.-C. Lai, and D. Keyser, 1995: A technique for diagnosing three-dimensional ageostrophic circulations in baroclinic disturbances on limited-area domains. *Mon. Wea. Rev.,* **123,** 1476–1504.

Lynch, P., 1989: Partitioning the wind in a limited domain. *Mon. Wea. Rev.,* **117,** 1492–1500.

Meade, D. A., 2001: Case studies of jet streak life cycles using potential vorticity concepts. M.S. thesis, Dept. of Earth and Atmospheric Sciences, University at Albany, State University of New York, 135 pp. [Available from Dept. of Earth and Atmospheric Sciences, University at Albany, State University of New York, Albany, NY 12222.]

Moore, J. T., and G. E. VanKnowe, 1992: The effect of jet-streak curvature on kinematic fields. *Mon. Wea. Rev.,* **120,** 2429–2441.

Morgan, M. C., and J. W. Nielsen-Gammon, 1998: Using tropopause maps to diagnose midlatitude weather systems. *Mon. Wea. Rev.,* **126,** 2555–2579.

Namias, J., and P. F. Clapp, 1949: Confluence theory of the high tropospheric jet stream. *J. Meteor.,* **6,** 330–336.

Newton, C. W., and A. Trevisan, 1984: Clinogenesis and frontogenesis in jet-stream waves. Part II: Channel model numerical experiments. *J. Atmos. Sci.,* **41,** 2735–2755.

Nielsen-Gammon, J. W., 2001: A visualization of the global dynamic tropopause. *Bull. Amer. Meteor. Soc.,* **82,** 1151–1167.

O'Brien, J. J., 1970: Alternative solutions to the classical vertical velocity problem. *J. Appl. Meteor.,* **9,** 197–203.

Orlanski, I., and J. P. Sheldon, 1995: Stages in the energetics of baroclinic systems. *Tellus,* **47A,** 605–628.

Palmén, E., and C. W. Newton, 1969: *Atmospheric Circulation Systems: Their Structure and Physical Interpretation.* International Geophysics Series, Vol. 13. Academic Press, 603 pp.

Pyle, M. E., 1997: A diagnostic study of jet streaks: Kinematic signatures and relationship to coherent tropopause disturbances. M.S. thesis, Dept. of Earth and Atmospheric Sciences, University at Albany, State University of New York, 169 pp. [Available from Dept. of Earth and Atmospheric Sciences, University at Albany, State University of New York, Albany, NY 12222.]

Riehl, H., and Coauthors, 1952: *Forecasting in Middle Latitudes. Meteor. Monogr.,* No. 5. Amer. Meteor. Soc., 80 pp.

Sanders, F., 1988: Life history of mobile troughs in the upper westerlies. *Mon. Wea. Rev.,* **116,** 2629–2648.

Saucier, W. J., 1955: *Principles of Meteorological Analysis.* The University of Chicago Press, 438 pp.

Schultz, D. M., and C. A. Doswell III, 1999: Conceptual models of upper-level frontogenesis in south-westerly and north-westerly flow. *Quart. J. Roy. Meteor. Soc.,* **125,** 2535–2562.

Shapiro, M. A., 1982: Mesoscale weather systems of the central United States. CIRES/NOAA Tech. Rep., University of Colorado, 78 pp. [Available from NCAR, P.O. Box 3000, Boulder, CO 80307-3000.]

Steers, J. A., 1970: *An Introduction to the Study of Map Projections.* 15th ed. University of London Press, 294 pp.

Sutcliffe, R. C., and A. G. Forsdyke, 1950: The theory and use of upper air thickness patterns in forecasting. *Quart. J. Roy. Meteor. Soc.,* **76,** 189–217.

Uccellini, L. W., and D. R. Johnson, 1979: The coupling of upper and lower tropospheric jet streaks and implications for the development of severe convective storms. *Mon. Wea. Rev.,* **107,** 682–703.

——, and P. J. Kocin, 1987: The interaction of jet streak circulations during heavy snow events along the east coast of the United States. *Wea. Forecasting,* **2,** 289–308.

——, ——, R. A. Petersen, C. H. Wash, and K. F. Brill, 1984: The Presidents' Day cyclone of 18–19 February 1979: Synoptic overview and analysis of the subtropical jet streak influencing the pre-cyclogenetic period. *Mon. Wea. Rev.,* **112,** 31–55.

——, D. Keyser, K. F. Brill, and C. H. Wash, 1985: The Presidents' Day cyclone of 18–19 February 1979: Influence of upstream trough amplification and associated tropopause folding on rapid cyclogenesis. *Mon. Wea. Rev.,* **113,** 962–988.

——, R. A. Petersen, K. F. Brill, P. J. Kocin, and J. J. Tuccillo, 1987: Synergistic interactions between an upper-level jet streak and diabatic processes that influence the development of a low-level jet and a secondary coastal cyclone. *Mon. Wea. Rev.,* **115,** 2227–2261.

Velden, C. S., and G. A. Mills, 1990: Diagnosis of upper-level processes influencing an unusually intense extratropical cyclone over southeast Australia. *Wea. Forecasting,* **5,** 449–482.

Wash, C. H., J. E. Peak, W. E. Calland, and W. A. Cook, 1988: Diagnostic study of explosive cyclogenesis during FGGE. *Mon. Wea. Rev.,* **116,** 431–451.